

# Weatherscapes: Nowcasting Heat Transfer and Water Continuity

JORGE ALEJANDRO AMADOR HERRERA, KAUST  
TORSTEN HÄDRICH, KAUST  
WOJTEK PAŁUBICKI, UAM  
DANIEL T. BANUTI, UNM  
SÖREN PIRK, Google Research  
DOMINIK L. MICHELS, KAUST



Fig. 1. Simulation of diverse weather conditions at the Sandia Mountains east of the city of Albuquerque in New Mexico. Using our framework, we can explore different ground and atmospheric settings. From left to right: snowfall, a foggy morning, cloudy warm afternoon, and a clear cold night.

Due to the complex interplay of various meteorological phenomena, simulating weather is a challenging and open research problem. In this contribution, we propose a novel physics-based model that enables simulating weather at interactive rates. By considering atmosphere and pedosphere we can define the hydrologic cycle – and consequently weather – in unprecedented detail. Specifically, our model captures different warm and cold clouds, such as mammatus, hole-punch, multi-layer, and cumulonimbus clouds as well as their dynamic transitions. We also model different precipitation types, such as rain, snow, and graupel by introducing a comprehensive microphysics scheme. The Wegener-Bergeron-Findeisen process is incorporated into our Kessler-type microphysics formulation covering ice crystal growth occurring in mixed-phase clouds. Moreover, we model the water run-off from the ground surface, the infiltration into the soil, and its subsequent evaporation back to the atmosphere. We account for daily temperature changes, as well as heat transfer between pedosphere and atmosphere leading to a complex feedback loop. Our framework enables us to interactively explore various complex weather phenomena. Our results are assessed visually and validated by simulating weatherscapes for various setups covering different precipitation events and environments, by showcasing the hydrologic cycle, and by reproducing common effects such as Foehn winds. We also provide quantitative evaluations creating high-precipitation cumulonimbus clouds by prescribing atmospheric conditions based on infrared satellite observations. With our model we can generate dynamic 3D scenes of weatherscapes with high visual fidelity and even nowcast real weather conditions as simulations by streaming weather data into our framework.

Authors' addresses: Jorge Alejandro Amador Herrera, KAUST, Visual Computing Center, Thuwal 23955, KSA; Torsten Hädrich, KAUST, Visual Computing Center, Thuwal 23955, KSA; Wojtek Pałubicki, UAM, Umultowska 87, 61-614 Poznań, Poland; Daniel T. Banuti, UNM, Mechanical Engineering, Albuquerque, NM 87131, USA; Sören Pirk, Google Research, 1600 Amphitheatre Parkway, Mountain View, CA, 94043, USA; Dominik L. Michels, KAUST, Visual Computing Center, Thuwal 23955, KSA.

Permission to make digital or hard copies of part or all of this work for personal or classroom use is granted without fee provided that copies are not made or distributed for profit or commercial advantage and that copies bear this notice and the full citation on the first page. Copyrights for third-party components of this work must be honored. For all other uses, contact the owner/author(s).

© 2021 Copyright held by the owner/author(s).  
0730-0301/2021/12-ART204

<https://doi.org/10.1145/3478513.3480532>

CCS Concepts: • **Computing methodologies** → **Physical simulation**.

Additional Key Words and Phrases: Cloud Simulation, Fluid Dynamics, Kessler Scheme, Mixed-phase Clouds, Physics-based Modeling and Simulation, Weather, Weatherscapes, Weather Simulation, Wegener-Bergeron-Findeisen Process.

## ACM Reference Format:

Jorge Alejandro Amador Herrera, Torsten Hädrich, Wojtek Pałubicki, Daniel T. Banuti, Sören Pirk, and Dominik L. Michels. 2021. Weatherscapes: Nowcasting Heat Transfer and Water Continuity. *ACM Trans. Graph.* 40, 6, Article 204 (December 2021), 19 pages. <https://doi.org/10.1145/3478513.3480532>

## 1 INTRODUCTION

Weather profoundly and consistently affects everyone's life on a daily basis. Understanding and modeling weather, to make reliable predictions, always has been of pivotal importance to mankind. This ranges from estimating weather conditions for agriculture or predicting natural disasters, to determining our daily behavior and activities. Commonly, weather is known as the state of the atmosphere established by various meteorological factors, such as temperature, precipitation, humidity, wind, and clouds. Essential to weather is the heat transfer between air and ground as well as the hydrologic cycle – the transport of water above and below the surface of the earth. Simulating the microphysics of water and its various state transitions is a shared and open problem across many research disciplines. Due to the involved complexity, most methods for simulating weather are based on complex mathematical models and numerical solvers that do not allow for exploring weather phenomena interactively. Furthermore, most methods do not focus on the visualization of weather phenomena. However, for many applications weather effects are an often crucial visual asset for content creation and story-telling alike.

Methods in computer graphics have mostly focused on modeling individual weather phenomena, such as clouds [Dobashi et al. 2008; Goswami and Neyret 2017; Harris et al. 2003; Vimont et al. 2020],

dynamic cloud transitions and thunderstorm supercells [Hädrić et al. 2020], rain [Garcia-Dorado et al. 2017], snow [Gissler et al. 2020], or lightning [Reed and Wyvill 1994]. Despite these advances in simulating weather phenomena, none of these methods proposes an integrated model of weather dynamics. However, real weather phenomena are caused by the complex interplay of various processes and cannot be plausibly simulated in isolation. By jointly simulating the microphysics of weather it is possible to describe the realistic transitions of weather patterns as well as their more accurate simulation.

Existing methods in climatology focus mostly on modeling weather at a macro-scale usually using spatial grids with step sizes of thousands of kilometers and temporal step sizes of months or even years. The main goal of many of these approaches is to precisely simulate weather with high-fidelity models to make reliable predictions [Houze 2014; Stocker 2011; Yau and Rogers 1996]. These methods often require significant amounts of computational resources and cannot be combined with other simulations or 3D world models. Furthermore, these methods do not focus on the visualization of weather phenomena, and they cannot be easily adapted to model weather effects at a micro-scale accurately capturing details which are present at spatial resolutions with step sizes of only a few kilometers and temporal step sizes of minutes or even fractions of seconds – such as a summer hail storm or the formation of specific cloud types.

While there is no universally accepted consensus what separates physics-based modeling and simulation at SIGGRAPH from its counterparts within the engineering and numerical methods disciplines, we consider it fair to point out that this type of research within the SIGGRAPH community is usually characterized by certain aspects. Among others, these comprise the development and demonstration of algorithms and models that can successfully operate in 3D at specific scales, show interactions with complex geometry, and demonstrate robustness and significant performance improvements compared to previous work. We perceive this combination of strengths within our community as a fruitful basis and a competitive profile to advance weather modeling next to only enabling the efficient visualization of weather phenomena, but also by providing an efficient means of exploring them based on the unique capacity of interactive 3D methods. Consequently, we consider our work relevant for both domain scientists as well as researchers in visual computing eager to contribute to the advancement of weather simulations. This requires an accurate representation of the physical processes underlying weather dynamics.

In this paper we introduce a novel physics-based model for weather simulation that enables the interactive simulation of weather phenomena. We propose novel mathematical formulations for the transfer of heat and water between the ground and the atmosphere. Radiative heat transfer is modeled by considering the ground albedo and the shadowing of clouds. To model water continuity we introduce a soil infiltration model that is integrated with the microphysics scheme of the atmosphere. Specifically, we represent water in various phases, such as liquid water, vapor, rain, ice, graupel, and snow. Furthermore, we consider the effect of the diurnal cycle on ground surface temperature. We showcase the capabilities of our complex

and realistic weather simulation approach by modeling the Foehn effect as well as advanced mixed-phase cloud formations.

Our framework supports the simulation of weather at interactive rates. Thereby it enables the nowcasting of real weather data as a realistic 4D simulation. Specifically, we use data of real-time weather services for priming our simulation to then explore the detailed progression of weather. Combining interactive simulations with online weather data is a novel way to understand and analyze weather phenomena. Moreover, a physically accurate simulation can be used to explore the complex feedback loop between ground surface and the atmosphere. To this end, we have combined our weather simulation with realistic representations of terrain obtained from real map data. Together, this allows us to generate dynamically changing and highly realistic outdoor scenes.

Our specific contributions are as follows: (1) We introduce a comprehensive first principle-based Kessler-type microphysics scheme that covers warm, cold, and mixed-phase clouds taking into account rain, snow and precipitated ice unifying previous research within a uniform framework. (2) We parametrize the underlying microphysics processes controlling the transformation between each cloud and precipitation type for given atmospheric conditions. (3) We include the analogous water content on the ground with their correspondent microphysical processes and couple it to our atmospheric water model. (4) We model solar and infrared radiation and their effects on the ground temperature. Cloud coverage is taken into account to include shading and greenhouse effects. (5) We introduce a low-dimensional set of parameters allowing to conveniently generate different weatherscapes. (6) We simulate complex weatherscapes for various setups to qualitatively validate our framework. Moreover, a quantitative evaluation is provided for high-precipitation cumulonimbus clouds based on infrared satellite observations. (7) We enable nowcasting of real weather conditions as simulations using weather data from external sources.

## 2 RELATED WORK

The mathematical modeling and simulation of different types of weather phenomena is an active and ongoing research topic within several academic communities. While this spans a breadth of work that we cannot conclusively discuss, we provide reference pointers to fluid dynamics, cloud and weather simulation, and atmospheric microphysics.

*Fluid Dynamics.* Since at least the seminal work of Stam [1999], the simulation of fluids is an established research focus within the computer graphics community. In this context, Bridson’s and Müller-Fischer’s SIGGRAPH course [2007] provided an introduction to fluid simulation from a computer graphics’ perspective. Moreover, Bridson [2015] provided a thorough explanation of grid based methods. While for many years no comparably established resource existed for particle-based techniques, Koschier et al. [2019] recently provided an excellent Eurographics tutorial on smoothed particle hydrodynamics techniques. Next to several methodological contributions improving the simulation of fluids such as, e.g., surface-only techniques [Da et al. 2016; Huang and Michels 2020] the computer graphics community has managed to continuously push the boundaries in fluid simulation by addressing an impressive portfolio of related

effects. This ranges from the simulation of intricate fluid phenomena such as vortical wakes and interacting vortex filaments [Chern et al. 2016], over bubble rings and ink chandeliers [Padilla et al. 2019], to magnetic fluids [Huang et al. 2019], and even the interaction of fluids and complex geometry [Pirk et al. 2017, 2014]. These days, machine learning is also utilized in fluid simulation as neural networks provide a powerful means to represent details of fluids, for example with an emphasis on temporal coherency [Xie et al. 2018], liquid splash modeling [Um et al. 2018], Lagrangian simulations [Ummenhofer et al. 2020], or style-transfer [Kim et al. 2020]. A variety of methods have been proposed for simulating ice and phase transitions [Kim and Lin 2003; Ren et al. 2018; Stomakhin et al. 2014; Xue et al. 2020].

*Cloud and Weather Simulation.* Physics-based simulations of clouds taking into account the underlying meteorological phenomena in the atmosphere have been the subjects of many contributions. One of the first methods has been presented by Kajiya and Von Herzen [1984] who introduced a dynamical model to generate realistic cloud animations. Several methods aiming for simulations at interactive rates rely on grid-based fluid solvers [Harris et al. 2003; Miyazaki et al. 2002; Overby et al. 2002]. A particle-based approach has been introduced by Goswami and Neyret [2017]. The procedural technique of Webanck et al. [2018] aims to model clouds while facilitating artistic control through user-defined keyframing. A method for simulating warm clouds on parallel GPU arrays has been proposed by Schalkwijk et al. [2015]. Given the large spatial extend in cloud simulations, refined representations are a natural choice and consequently have been subjects of previous contributions covering geometric- and particle-based representations [Bouthors and Neyret 2004; Gardner 1985; Neyret 1997], position-based dynamics [Ferreira Barbosa et al. 2015], and layer-based approaches [Vimont et al. 2020]. Vimont et al. also provided a thorough overview of existing methods w.r.t. simulated cloud types and scales. On a different trajectory, Hädrich et al. [2021] recently addressed the simulation of so-called flammagenitus clouds which occur in the context of wildfires. Next to the simulation of clouds, several weather phenomena have been addressed within the computer graphics community. The spectrum ranges from large-eddy simulations [Griffith et al. 2009], rain [Garcia-Dorado et al. 2017] and snow [Gissler et al. 2020], over lightning [Reed and Wyvill 1994], to thunderstorm supercells [Hädrich et al. 2020].

*Atmospheric Microphysics.* Since Kessler’s [1995] pioneering work on the distribution and continuity of water substance in atmospheric circulations, a number of microphysics parametrizations have been introduced modeling several phenomena such as cloud seeding precipitation enhancement, and the effect of aerosols on cold cloud formations. Rutledge and Hobbs [1983] studied the seeder-feeder process in warm-frontal rainbands and Schultz [1995] addressed water phase change and precipitation processes in warm clouds. Rutledge and Hobbs [1984] provided a diagnostic modeling study of precipitation development in narrow cold-frontal rainbands. Hsie et al. [1980] included mixed-phase clouds but only covered rain and ice as precipitation. Kärcher and Burkhardt [2008] employed microphysics for warm and cold clouds but their model is limited due to a statistical representation of the Wegener–Bergeron–Findeisen

(WBF) process which covers ice crystal growth occurring in mixed-phase clouds. None of these models includes interactions with the ground.

There are multiple parametrizations of mixed-phase clouds specifically addressing the WBF process. Some parametrizations are built empirically based on measured data such as the Beijing Climate Center Climate System Model (BCC-CSM [2010]), the interpolation presented by Pithan et al. [2014], the Institut Pierre Simon Laplace Model (IPSC-CM5A [2013c]), the National Centre for Meteorological Research Model (CNRM [2013a]), the Russian Institute for Numerical Mathematics Climate Model (INMCM4 [2010]), and the Model for Interdisciplinary Research on Climate Model (MIROC-ESM [2011]). They basically parametrize the WBF process as an interpolation of average ice fraction at certain temperatures. Within the Goddard Institute for Space Studies Model (GISS-E2-R [2006]) a probability distribution of ice fraction as a function of temperature is employed. We build our model based on the stratiform-cloud and precipitation scheme introduced by Rotstayn [1997]. On a different trajectory, we would like to mention that the current version of the popular European Centre Hamburg Model (ECHAM6 [2013b]) couples microphysics with radar data taking into account the albedo as well as absorptions and reflections of clouds with themselves.

### 3 OVERVIEW

The principal motivation for our approach is to realistically model and simulate local weather dynamics, particularly, the microphysics of water continuity above and below the surface of the earth. This is a challenging task because of the complex interplay of heat and fluid dynamics at atmospheric and ground levels, which includes multiple water phase transitions, heat transfer on the atmosphere, and the presence of wind fields and the diurnal cycle that controls energy flow on the earth.

We address these challenges by employing an integrated model based on first principles that distinguishes between three cloud types (warm clouds composed of liquid water, cold clouds formed by ice crystals, and mixed-phase clouds in which both supercooled water and ice crystals co-exist<sup>1</sup>) as well as three types of precipitation (rain, snow and precipitated ice). We parametrize the microphysics processes that control the transformation between each cloud and precipitation type depending on atmospheric conditions. Moreover, we also include the analogous water content on the ground (rainfall, ice, snow and infiltrated water) with their correspondent microphysical processes and couple it to our atmospheric water model by implementing infiltration and evaporation processes. Thermo- and fluid dynamics are introduced by means of a wind field and an atmospheric heat transfer model. Finally, we simulate both solar and infrared radiation and their effects on the ground temperature. Moreover, we couple cloud coverage to this dynamics so that we can consider the shading and greenhouse effect of clouds. While our model includes the parametrization of several phenomena, we introduce a canonical set of parameters (ground temperature  $T_G$ ,

<sup>1</sup>We use the water-phase cloud classification [Pruppacher and Klett 2012] to distinguish the microphysics in each species. However, our model handles low, middle, and high altitude clouds.

subsurface water content  $q_{sr}$ , average solar irradiance  $\bar{P}$ , and a material map that controls soil type) that allows to easily explore different weatherscapes.

In the following sections we introduce our model and showcase its capabilities by simulating mixed-phase cloud formation and precipitation, local weather phenomena and diverse weatherscapes. Finally, we explore the nowcasting capabilities of our model by coupling our framework with weather data and comparing the temperature evolution in our simulation with real measurements.

## 4 METHODOLOGY

In this section we present an overview of our local weather dynamics model, which can be divided into a ground thermodynamics model that describes the earth's diurnal temperature cycle, an infiltration model that determines surface and subsurface water content, a microphysics scheme that describes the creation and transformation between different cloud and precipitation types above the ground, and the fluid dynamics model which determines the motion of humid air in the atmosphere.

### 4.1 Atmosphere

Following Hädrich et al. [2020], our atmospheric model includes a reference temperature and pressure distributions for the surrounding dry air as well as a local thermodynamic model of the rising thermal of humid air.

**4.1.1 Atmospheric Conditions.** In our model we implement the temperature at ground level as a dynamic variable  $T_G = T_G(x, y, t)$ . The atmospheric temperature profile [Atmosphere 1975] is given by

$$T(x, t) = \begin{cases} T_G(x, y, t) + \Gamma_0 z, & \text{if } 0 \leq z \leq z_1, \\ T_G(x, y, t) + \Gamma_0 z_1 + \Gamma_1 (z - z_1), & z_1 \leq z \end{cases} \quad (1)$$

with a lapse rate  $\Gamma_0$  and a second lapse rate  $\Gamma_1$  for simulating an inversion layer at higher altitude. From this profile and the fundamental hydrostatic equation [Houze 2014] we obtain the corresponding pressure distribution

$$p(x, t) = p_G \left( 1 - \frac{\Gamma z}{T_G(x, y, t)} \right)^{\frac{g}{RT(x, t)}}, \quad (2)$$

where  $p_G$  is the pressure at ground level,  $g = 9.81 \text{ m s}^{-2}$  is the acceleration of gravity, and the specific gas constant  $R = \mathcal{R}/\mathcal{M}_{\text{air}}$  is the ratio of the universal gas constant  $\mathcal{R} = 8314 \text{ J g}^{-1} \text{ K}$  and the molar mass of dry air  $\mathcal{M}_{\text{air}} = 28.96 \text{ g mol}^{-1}$ .

**4.1.2 Rising Thermal.** The thermal, a column of rising humid air composed of water vapor and dry air, has an average molar mass

$$\mathcal{M}_{\text{th}} = X_V \mathcal{M}_{\text{water}} + (1 - X_V) \mathcal{M}_{\text{air}} \quad (3)$$

with the water vapor mole fraction  $X_V$  and the water molar mass  $\mathcal{M}_{\text{water}} = 18.02 \text{ g mol}^{-1}$ . Mass fractions  $Y$  and mole fractions  $X$  are related through

$$Y_V = X_V \frac{\mathcal{M}_{\text{water}}}{\mathcal{M}_{\text{th}}}. \quad (4)$$

The amount of water in the atmosphere can also be expressed in terms of the mass ratio  $q_j$  of water per mass unit of dry air, specifically vapor  $q_v$ , liquid water cloud  $q_w$ , ice cloud  $q_c$ , rain  $q_r$ , snow

$q_s$ , and precipitated ice  $q_i$ . Mole fractions  $X_j$  are related to the mass ratios  $q_j$  via

$$X_j = \frac{q_j}{q_j + 1}. \quad (5)$$

**4.1.3 Thermodynamics of the Thermal.** The thermal rises as a result of its density difference with respect to surrounding dry air. Its expansion is slow enough that it can be assumed to be isentropic, and heat exchange with the background atmosphere can be neglected. From the isentropic relations [Anderson 2003] we can determine the temperature change due to the change in pressure as

$$T_{\text{th}}(x, t) = T_G(x, y, t) \left( \frac{p(x, t)}{p_G} \right)^{\frac{\gamma_{\text{th}} - 1}{\gamma_{\text{th}}}} \quad (6)$$

with an isentropic exponent of the humid thermal

$$\gamma_{\text{th}} = Y_V \gamma_V + (1 - Y_V) \gamma_{\text{air}} \quad (7)$$

with isentropic exponents  $\gamma_{\text{air}} = 1.4$  and  $\gamma_V = 1.33$  for air and water vapor, respectively. From Archimedes' principle, this density difference between the thermal of volume  $V$  and the surrounding air will result in a vertical lift  $L = Vg(\rho_{\text{air}} - \rho_{\text{th}})$ . Combining this with Newton's second law  $F = ma$  and the ideal gas relation  $RT\rho = p$ , we obtain the buoyancy acceleration on the thermal as

$$B(x, t) = g \left( \frac{\mathcal{M}_{\text{air}} T_{\text{th}}(x, t)}{\mathcal{M}_{\text{th}} T_{\text{air}}(x, t)} - 1 \right). \quad (8)$$

### 4.2 Microphysical Processes

We distinguish between three cloud types: warm clouds made up of condensed water droplets, cold clouds which are composed of ice crystals, and mixed-phase clouds in which both supercooled water droplets and ice coexist. Additionally, we treat three types of precipitation: rain, snow and precipitated ice, which encompasses graupel, hail and sleet. Our microphysics model, represented schematically in Figure 2, includes an extra system of coupled transport equations to account for the several physical interactions between the cloud types and precipitation types. Using the material derivative  $D_t \phi = \partial \phi / \partial t + \mathbf{v} \cdot \nabla \phi$  [Kundu et al. 2012], we can write

$$D_t q_v = E_W + S_C + E_R + E_I + E_S + E_G - C_W - D_C, \quad (9)$$

$$D_t q_w = C_W + M_C - E_W - A_W - K_W - R_W - F_W - B_W, \quad (10)$$

$$D_t q_c = D_C + F_W + B_W - S_C - A_C - K_C - M_C, \quad (11)$$

$$D_t q_r = A_W + K_W + M_S + M_I - E_R - F_R - G_R, \quad (12)$$

$$D_t q_s = A_C + K_C - M_S - E_S - R_S - G_S, \quad (13)$$

$$D_t q_i = F_R + R_S + R_W - E_I - M_I - G_I \quad (14)$$

with the source terms for condensation  $C_W$ , deposition  $D_C$ , sublimation  $S_C$ , evaporation  $E$  of the different water types,  $R$  describing rimming processes,  $A$  describing the autoconversion of cloud matter into precipitation,  $K$  describing the accretion of cloud matter by either snow or rain, and  $F$  describing freezing. A detailed list of the symbols used in this parametrization can be found in Appendix A.

**4.2.1 Warm Clouds.** The rising thermal will cool down until the partial pressure on its water vapor content drops below the saturation pressure at the local temperature. At that point, the excess water vapor that cannot be solved in the air condenses into the tiny

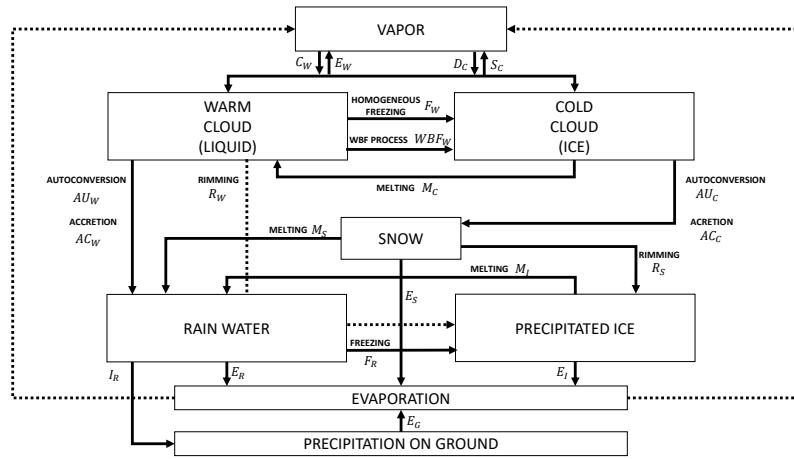


Fig. 2. Illustration of our microphysics scheme for modeling the water transport between different cloud and precipitation types.

droplets that compose a warm cloud. Equilibrium vapor pressure over liquid water can be computed via the Magnus approximation:

$$e_w(T) = 611.2 \exp \left[ \frac{17.62T}{T + 243.12} \right], \quad (15)$$

for a given temperature in Celsius [Alduchov and Eskridge 1996]. The limit vapor pressure is directly proportional to the vapor mixing ratio  $e = 1.607q_v p$ , with the pressure  $p$  in Pascal [Yau and Rogers 1996]. Combining both equations results in an expression for the saturation vapor mixing ratio over water

$$q_{ws}(T, p) = \frac{380.16}{p} \exp \left[ \frac{17.67T}{T + 243.50} \right]. \quad (16)$$

Following Hädrich et al. [2020], we use

$$E_W - C_W = \min(q_{ws} - q_v, q_w) \quad \text{for } T \geq -40, \quad (17)$$

where we added the temperature dependence because warm cloud matter exists only for temperatures above  $-40^\circ\text{C}$ . All of its water content is frozen at lower temperatures.

**4.2.2 Mixed-Phase Clouds.** When the warm cloud reaches an altitude where the temperature is below  $0^\circ\text{C}$ , ice crystals will start to form if the pressure drops below the equilibrium vapor pressure over ice at the local temperature. Moreover, in the temperature range from  $-40^\circ\text{C}$  to  $0^\circ\text{C}$ , supercooled water can still exist in its liquid state. Since the equilibrium vapor pressure over liquid water  $e_w$  is higher than the equilibrium vapor pressure over ice  $e_i$ , all liquid water is evaporated while there is rapid ice crystal growth through vapor deposition. This is usually denoted as the Wegener-Bergeron-Findeisen (WBF) process. To parametrize this phenomena in terms of its microphysical processes we make two assumptions. First, cloud ice is assumed to be uniformly mixed with the water content inside the cloud. Also, ice particles are treated as if they were hexagonal plates. The rate constant for vapor deposition on hexagonal crystals  $c_{vd}$  is given by Rotstajn [1997]:

$$c_{vd} = 65.2 \frac{N_i^{1/2} (e_w - e_i)}{\rho_{\text{air}}^{1/2} (A + B) e_i}, \quad (18)$$

where  $N_i$  is the ice crystal number concentration and the saturation ratios  $A$  and  $B$  represent heat conduction and vapor diffusion, respectively, and are computed as

$$A = \frac{L_s}{K_a T} \left( \frac{L_s}{R_v T} - 1 \right), \quad (19)$$

$$B = \frac{R_v T p}{2.21 e_i} \quad (20)$$

with the thermal conductivity of air  $K_a = 2.40 \times 10^{-2} \text{ J m}^{-1} \text{ s}^{-1} \text{ K}^{-1}$ , the specific gas constant for water vapor  $R_v = 461 \text{ J kg}^{-1} \text{ K}^{-1}$ , and the latent heat of sublimation of water  $L_s = 2.834 \times 10^6 \text{ J kg}^{-1}$ . The concentration of available ice crystals for the nucleation process is a function of ice supersaturation [Meyers et al. 1992], so that

$$N_i = 10^3 \exp \left[ \frac{12.96(e_w - e_i)}{e_i - 0.639} \right]. \quad (21)$$

As ice grows by vapor deposition, liquid water cloud content  $q_c$  will evaporate to keep the air at saturation with respect to liquid water. Thus, the ice content increases at the expense of liquid water being evaporated from the cloud, and the complete phase transition can be modeled as freezing. Following Rotstajn [2000], the amount of warm cloud that will be converted to ice cloud via this process is

$$B_W = \min \left[ q_w, \left( (1 - \alpha) c_{vd} \Delta t + \tilde{q}^{1-\alpha} \right)^{\frac{1}{1-\alpha}} - q_i \right] \quad (22)$$

for  $-40^\circ\text{C} \leq T \leq 0^\circ\text{C}$ , with the capacitance for hexagonal crystals  $\alpha = 0.5$ , and the local value of cloud ice mixing ratio for an uniformly distributed mixed-phase cloud

$$\tilde{q} = \max \left[ \frac{10^{-12} N_i}{\rho_{\text{air}}}, q_i \right]. \quad (23)$$

Magnus approximation for equilibrium vapor pressure over ice is

$$e_i(T) = 611.2 \exp \left[ \frac{24.46T}{T + 272.62} \right] \quad (24)$$

at a given temperature  $T$  in Celsius [Yau and Rogers 1996].

**4.2.3 Cold Clouds.** At temperatures below  $-40^\circ\text{C}$ , homogeneous nucleation will occur naturally. This causes all the remaining liquid water content on the cloud to experience isobaric freezing [Pruppacher and Klett 2012] and thus transforms the mixed-phase cloud entirely into an ice cloud. Accordingly, we set

$$F_W = q_w \quad \text{for } T \leq -40^\circ\text{C}, \quad (25)$$

representing the sudden freezing of the remaining water content on the cloud. Analogously, at temperatures above  $0^\circ\text{C}$ , all the ice cloud matter will melt into water liquid content, so that

$$M_C = q_c \quad \text{for } T \geq 0^\circ\text{C}. \quad (26)$$

For this transition from warm to cold clouds we assumed that the atmospheric air was already supersaturated with respect to liquid water ( $q_c \neq 0$ ). When this is not the case and the rising thermal reaches this altitude ( $T < 0^\circ\text{C}$ ), it will supersaturate with respect to ice. From Magnus approximation for the equilibrium vapor pressure over ice we get the saturation vapor mixing ratio over ice

$$q_{is}(T, p) = \frac{380.16}{p} \exp\left[\frac{24.46T}{T + 272.62}\right]. \quad (27)$$

We then apply

$$D_C - S_C = \min(q_{is} - q_v, q_c) \quad \text{for } T \leq 0^\circ\text{C}. \quad (28)$$

**4.2.4 Collection by Precipitation.** Rain is produced when the cloud liquid concentration increases to the point where collision among cloud droplets results in drops large enough to fall. Following Hädrich et al. [2020] we set

$$A_W = \beta_{A_W} \max(q_w - q_{w_{\min}}, 0) \quad (29)$$

with  $q_{w_{\min}} = 0.001 \text{ kg kg}^{-1}$  being the minimum cloud water content required before rainmaking begins, and constant  $\beta_{A_W}$ . Once raindrops form, they will grow faster by sweeping out cloud droplets as they fall. This accretion process is expressed as

$$K_W = \beta_{K_W} q_w q_r \quad (30)$$

with constant  $\beta_{K_W}$  [Kessler 1995]. Analogously, snow is produced when cloud ice concentrations exceed a threshold, indicating that cloud ice particles have either aggregated to form snowflakes or grown by diffusion to have appreciable fall velocities, so we apply

$$A_C = \beta_{A_C} \max(q_c - q_{c_{\min}}, 0) \quad (31)$$

with the threshold  $q_{c_{\min}} = 0.001 \text{ kg kg}^{-1}$  and rate coefficient  $\beta_{A_C}$ . The efficiency of cold cloud autoconversion depends on the crystal size which, in turn, depends on temperature, so, according to [Lin et al. 1983], the coefficient is given by

$$\beta_{A_C}(T) = 10^{-3} \exp[0.025T]. \quad (32)$$

The accretion of cold cloud by snow is simply

$$K_C = \beta_{K_C} q_c q_s \quad (33)$$

with constant  $\beta_{K_C}$ . Precipitated ice (i.e. graupel, sleet, and hail) is produced in three ways. The first is in mixed-phase clouds, where it grows by the rimming between ice crystals and cloud liquid water. This microphysics process is similar to the accretion processes [Morrison et al. 2015], so that

$$R_W = \beta_{R_W} q_i q_w \quad (34)$$

with constant  $\beta_{R_W}$ . Similarly, rimming snow can also produce precipitated ice in mixed-phase clouds, with a collection equation

$$R_S = \beta_{R_S} q_s q_w \quad (35)$$

with the addition that, in general,  $\beta_{R_S} > \beta_{R_W}$ , to account for the fact that snow collects cloud water more efficiently than ice particles [Hong et al. 2004]. The third mechanism for producing precipitating ice is the freezing of rain. Cotton [1972] suggests that freezing of raindrops is a temperature dependent process described by a parabolic function starting at  $-8^\circ\text{C}$  and negligible for warmer temperatures. Accordingly, we apply

$$F_R = \beta_{F_R} (T + 8)^2 \quad \text{for } T \leq -8^\circ\text{C}. \quad (36)$$

**4.2.5 Precipitation melting.** We constrain the total amount of melting (cold cloud, snow, and precipitating ice) in a time step so that the latent heat consumed does not lower the local temperature below the freezing point

$$\delta(X_c + X_s + X_i) \leq \frac{c_{p_{\text{air}}}}{L_f} T, \quad (37)$$

where  $c_{p_{\text{air}}}$  is the heat capacity of dry air at constant pressure and  $L_f$  is the latent heat of fusion. Moreover, we assume that less massive particles melt faster than larger particles, so that in the constrain we first melt cloud ice, then snow and finally precipitating ice, following the average ice crystal size distributions for each ice type [Fletcher 2011]. Just as cold clouds, we assume that snow melts instantaneously:

$$M_S = q_s \quad \text{for } T \geq 0^\circ\text{C}. \quad (38)$$

However, precipitated ice can fall considerable distances through air warmer than its melting point [Dudhia 1989], so its melting rate is modeled as a linear function of temperature

$$M_I = \beta_{M_I} T \quad \text{for } T \geq 0^\circ\text{C} \quad (39)$$

with constant  $\beta_{M_I}$ .

**4.2.6 Evaporation of Precipitation.** Small particles evaporate before large particles and liquid evaporates before ice. Consequently, we first evaporate warm cloud matter, then rain, cold cloud matter, snow, and finally precipitated ice. While warm and cold clouds evaporate instantly, precipitation types evaporate at rates proportional to the vapor deficit relative to the saturation mixing ratio of ice and liquid water [Dudhia 1989]. We then apply

$$E_R = \beta_{E_R} \max[q_{ws} - q_v, 0], \quad (40)$$

$$E_S = \beta_{E_S} \max[q_{is} - q_v, 0], \quad (41)$$

$$E_I = \beta_{E_I} \max[q_{is} - q_v, 0] \quad (42)$$

with constants  $\beta_{E_R}$ ,  $\beta_{E_S}$ , and  $\beta_{E_I}$ . Evaporation occurs when there is a vapor deficit relative to the corresponding saturation mixing ratio, so we constrain the amount of water evaporation in a time step

$$\delta(q_w + q_r) \leq q_{ws} - q_v, \quad (43)$$

as well as the total ice evaporation

$$\delta(q_c + q_s + q_i) \leq q_{is} - q_v. \quad (44)$$

**4.2.7 Falling Velocities.** We model the terminal falling speed of each precipitation types as a function of its mixing ratio. Assuming an exponential distribution for the diameter of each precipitation particle we obtain mass-weighted mean terminal velocities

$$U_R = a \frac{\Gamma(4+b)}{6\lambda_R^b} \sqrt{\frac{\rho_{\text{water}}}{\rho_{\text{air}}}}, \quad (45)$$

$$U_S = c \frac{\Gamma(4+d)}{6\lambda_S^d} \sqrt{\frac{\rho_{\text{snow}}}{\rho_{\text{air}}}}, \quad (46)$$

$$U_I = \sqrt{\frac{4}{3C_D}} \frac{\Gamma(4,5)}{6\lambda_I^{0.5}} \sqrt{\frac{g\rho_{\text{ice}}}{\rho_{\text{air}}}} \quad (47)$$

for rain, snow, and precipitated ice, respectively, with gamma function  $\Gamma(x)$  and incomplete gamma function  $\Gamma(x, y)$ . The derivation is given in Appendix B.

**4.2.8 Heat Transfer from Microphysical Processes.** Whenever there is a phase transition of the water content, an associated heat release or absorption takes place, so we must extend the temperature equation of the thermal (6) accordingly. The energy release in a phase transition  $a$  per water mass fraction  $X_j$  is the corresponding latent heat  $L_a$  of the transition. Then, in general, the additional temperature change has the form

$$\delta T_a = \frac{L_a}{c_p^{\text{th}}} X_j \quad (48)$$

with heat capacity  $c_p^{\text{th}}$  of the gaseous part of the thermal which is composed of dry air and water vapor  $X_V$ . We obtain

$$c_p^{\text{th}} = \frac{\gamma_{\text{th}} \mathcal{R}}{\mathcal{M}_{\text{th}} (\gamma_{\text{th}} - 1)} \quad (49)$$

using the thermal average molar gas as calculated in (3), and its isentropic exponent (7). The thermal temperature equation is then extended as

$$T_{\text{th}}(\mathbf{x}) = T_G(\mathbf{x}) \left( \frac{p(z)}{p_G} \right)^{\frac{\gamma_{\text{th}}-1}{\gamma_{\text{th}}}} + \sum_a \frac{L_a}{c_p^{\text{th}}} X_j, \quad (50)$$

where we sum over all phase transitions described in the previous section.

### 4.3 Ground Model

To account for the additional physical processes that take place within the hydrologic cycle, we also model the water dynamics and thermodynamics at surface and subsurface levels.

**4.3.1 Precipitation in the Ground.** Once cloud content precipitates and falls at ground level  $z = z_0$ , it will accumulate on the surface as ground snow  $q_{gs}$ , ground precipitated ice  $q_{gi}$ , and ground rain water  $q_{gr}$ . The microphysics processes of precipitation accumulated on the ground are modeled as

$$d_t q_{gr} = G_R + M_S + M_I - E_R - F_R - I_R, \quad (51)$$

$$d_t q_{gs} = G_S - M_S - E_S, \quad (52)$$

$$d_t q_{gi} = G_I + F_R - E_I - M_I, \quad (53)$$

where rimming, accretion, and autoconversion processes are not considered since there are no clouds in the ground. Moreover, we

take the usual derivative instead of the material derivative because precipitation in the ground does not move with the thermal. The terms  $G_R = q_r$ ,  $G_S = q_s$ , and  $G_I = q_i$  represent the precipitation amount that has reached the ground. While snow and precipitated ice in the ground will only change due to their microphysical processes, rain water will also move by diffusion and by the slopes at the surface of the ground. Hence, (51) is extended to

$$d_t q_{gr} = D_G \nabla^2 q_{gr} + v \frac{\delta q_{gr}}{\delta t} + G_R + M_S + M_I - E_R - F_R - I_R \quad (54)$$

with the diffusion coefficient for ground rain water  $D_G$  and the advection term  $v \delta q_{gr} / \delta t$  in which  $v$  represents the downhill flow rate, and  $\delta q_{gr} / \delta t$  is the slope, computed as the height difference of the current position and its neighbors given a terrain height map (Section 5.1). Additionally, a fraction of the rain water at surface level will infiltrate into the ground as subsurface rain water  $q_{sr}$ , such that

$$d_t q_{sr} = D_S \nabla^2 q_{sr} + v \frac{\delta q_{sr}}{\delta t} + I_R - E_G, \quad (55)$$

where  $D_S$  is the diffusion coefficient for subsurface water,  $I_R$  describes surface water infiltration and  $E_G$  is the evaporation rate of subsurface water. General flow through porous media is described with the Richards equation. However, it can be shown [Ross and Parlange 1994] that, in the long time evolution, this equation can be reduced to Horton's approximation [Horton 1941] of the steady state infiltration rate, for which

$$I_R = \beta_{I_R} \kappa q_{gr} \quad (56)$$

with constant  $\beta_{I_R}$  and the hydraulic conductivity of the ground  $\kappa$ . Finally, the evaporation rate from drying ground can be approximated as

$$E_G = \beta_{E_G} \bar{D} q_{sr} \exp(-t/24\phi), \quad (57)$$

where  $\beta_{E_G}$  is the evaporation rate constant,  $\bar{D}$  is the weighted mean diffusivity of the ground, and  $\phi$  is the evaporative ground water storage coefficient [Brutsaert 2014]. The ground is drying when there is no precipitation or surface water on top of it [Lal and Shukla 2004], so we only apply  $E_G$  at zones where  $q_{gj} = 0$  for all precipitation types  $j$ , and we restart the  $t$  parameter after a precipitation event.

**4.3.2 Heat Transfer at the Ground.** The microphysical processes that take place at the ground surface and subsurface level will affect the local temperature of the ground  $T_G$ . When there is a phase transition  $a$  per water mass fraction  $X_j$  in the ground with heat capacity  $c_p^G$ , the temperature change is given by

$$\delta T_a = \frac{L_a}{c_p^G} X_j. \quad (58)$$

**4.3.3 Daily Temperature Changes.** Solar irradiance is the power per unit area received from the sun  $P = (1/A)dQ/dt$  and is, ultimately, a function of the solar cycle, distance to the sun and other astronomical parameters. However, variations in incoming solar radiation during daytime can be approximated by assuming that solar irradiance oscillates as a pure harmonic function of time around an average (monthly or yearly) irradiance  $\bar{P}$  [Lal and Shukla 2004]. We

can then express the irradiance each hour as

$$P(t) = \bar{P} \max \left[ \sin \left( \frac{\pi}{2} \left( 1 - \frac{t-s-d/2}{d/2} \right) \right), 0 \right] \quad (59)$$

with the daylight duration  $d$  and hour of sunrise  $s$ . This is the irradiance when all the solar radiation has been absorbed. However, a fraction of the solar radiation will be reflected by clouds on top of the ground due to their high albedo. To model this phenomenon we define the local cloud covering fraction  $L_C$  as

$$L_C(x, y, t) = \min \left[ \frac{\int_0^{z_n} (q_c + q_w) dz}{q_{\text{full}}}, 1 \right] \quad (60)$$

where  $\int_0^{z_n} (q_c + q_w) dz$  is the total cloud content on top of  $(x, y)$  and  $q_{\text{full}}$  is a threshold value where all incoming radiation is reflected by cloud matter. Suitable values for  $q_{\text{full}}$  were based on the measurements of Li et al. [1995] and Lubin et al. [1996]. The energy change on the ground is given by

$$\frac{dQ}{dt} = AP(x, y, t) = (1 - \alpha)(1 - L_C)AP(t), \quad (61)$$

where we also take into account that only a fraction of the radiation that reached the ground will be absorbed depending on its albedo  $\alpha$ . While incoming solar radiation heats the ground, there is also an energy loss due to infrared radiation emission. Following the Stefan-Boltzmann law, the power radiated by a body with surface area  $A$  at temperature  $T$  can be expressed by

$$\frac{dQ}{dt} = (1 - L_C)A\epsilon\sigma T^4 \quad (62)$$

with the emissivity  $\epsilon$  of the body and the Boltzmann constant  $\sigma = 5.67 \times 10^{-8} \text{ W m}^{-2} \text{ K}^{-4}$ . We also included the factor of cloud content to account for the fraction of the radiation that is bounced back to the ground by the clouds on top of it. Combining (61) and (62) we obtain the temperature change in a ground section of surface area  $A$ , thickness  $w$  and heat capacity  $c_p^G$  due to both incoming solar radiation and infrared emission as

$$\delta T_{\text{daily}} = \frac{dQ}{mc_p^G} = (1 - L_C) \frac{(1 - \alpha)P(t) - \epsilon\sigma T^4}{w\rho_G c_p^G}, \quad (63)$$

where  $\rho_G$  is the density of the ground. The total temperature change is then

$$\frac{dT_G}{dt} = (1 - L_C) \frac{(1 - \alpha)P(t) - \epsilon\sigma T^4}{w\rho_G c_p^G} + \sum_a \frac{L_a}{c_p^G} X_j. \quad (64)$$

Since heat transfer at ground level via diffusion and convection occurs at spatial and temporal scales much smaller than the processes modeled in our approach, we do not take it into account. Nonetheless, including such processes would improve the accuracy and realism of local temperature evolution in our framework, but it is left for future work.

#### 4.4 Fluid Dynamics

The state of the thermal is described by a velocity field  $\mathbf{u} : (\mathbf{x}, t) \rightarrow \mathbf{u}(\mathbf{u}, t)$  which, given a time  $t \in \mathbb{R}^+$  and a position  $\mathbf{x}$ , returns the local

flow  $\mathbf{u}(\mathbf{u}, t) \in \mathbb{R}^3$ . The temporal evolution of  $\mathbf{u}$  is described by the Navier-Stokes equation [Bridson 2015]

$$\frac{\partial \mathbf{u}}{\partial t} + \mathbf{u} \cdot \nabla \mathbf{u} + \frac{1}{\rho_{\text{air}}} \nabla p = \nu \nabla^2 \mathbf{u} + \mathbf{b} + \mathbf{f} \quad (65)$$

with air density  $\rho_{\text{air}}$ , pressure  $p$ , buoyancy  $\mathbf{b}$ , kinematic viscosity  $\nu$  and any other external forces combined in  $\mathbf{f}$ . The conservation of mass under constant density prescribes the continuity equation as

$$\nabla \cdot \mathbf{u} = 0. \quad (66)$$

Finally, energy conservation in temperature form can be written [Houze 2014] as

$$\frac{\partial \theta}{\partial t} + (\mathbf{u} \cdot \nabla) \theta = \sum_a \frac{L_a}{c_p \Pi} X_j, \quad (67)$$

where  $\Pi = T(t_0)/\theta$  is the ratio of the absolute and the potential temperature as described by Hädrićh et al. [2020].

## 5 ALGORITHMICS

The atmospheric and ground models described in the previous section provide the basis of our simulation framework. The procedure is summarized in Algorithm 1. Additionally, Figure 3 presents an overview of our model pointing out interdependencies.

---

**ALGORITHM 1:** Overview of our numerical procedure.

---

**Input:** Current system state.

**Output:** Updated system state.

**1 Procedure:**

2 Update total incoming solar radiation according to (59).

3 **for each**  $(x, y, \mathcal{H}(x, y)) \in \partial\Omega_{\text{bottom}}$  **do**

4 | Compute cloud covering fraction  $L_C(x, y)$  according to (60).

5 | Update ground temperature  $T_G(x, y)$  following (63).

6 | Diffuse and advect water content  $q_{jg}$  as described in (52)–(55)

7 | Update microphysics processes of  $q_{jg}$  according to (52)–(55).

8 | Compute heat transfer at ground level  $T_G(x, y)$  due to phase transitions following (58).

9 **end**

10 **for each**  $\mathbf{x} \in \Omega$  **do**

11 | Update atmospheric temperature  $T(\mathbf{x})$  according to (1).

12 | Diffuse, advect and pressure project temperature  $\theta$ , field  $\mathbf{u}$

13 | and atmospheric water content  $q_j$  following the Eulerian solver of Hädrićh et al. [2020] including water transfer between ground and atmosphere, as well as vorticity confinement.

14 | Update microphysics processes of  $q_j$  using (9)–(14).

15 | Compute heat transfer  $\theta(\mathbf{x})$  due to phase transitions as

16 | described by (67).

17 **end**

---

### 5.1 Numerical Procedure

We distinguish between computations within our atmospheric spatial domain  $\Omega \in \mathbb{R}^3$  and those at ground level  $\partial\Omega_{\text{bottom}}$ . Accordingly, we set up a 3D voxel space using a uniform grid scale  $\Delta x$  in which we store the current state of the atmospheric system (which corresponds to the mixing ratios  $q_j$ , potential temperature  $\theta$ , and the velocity field  $\mathbf{u}$ ) and a 2D uniform grid with the same scale  $\Delta x$  for storing the

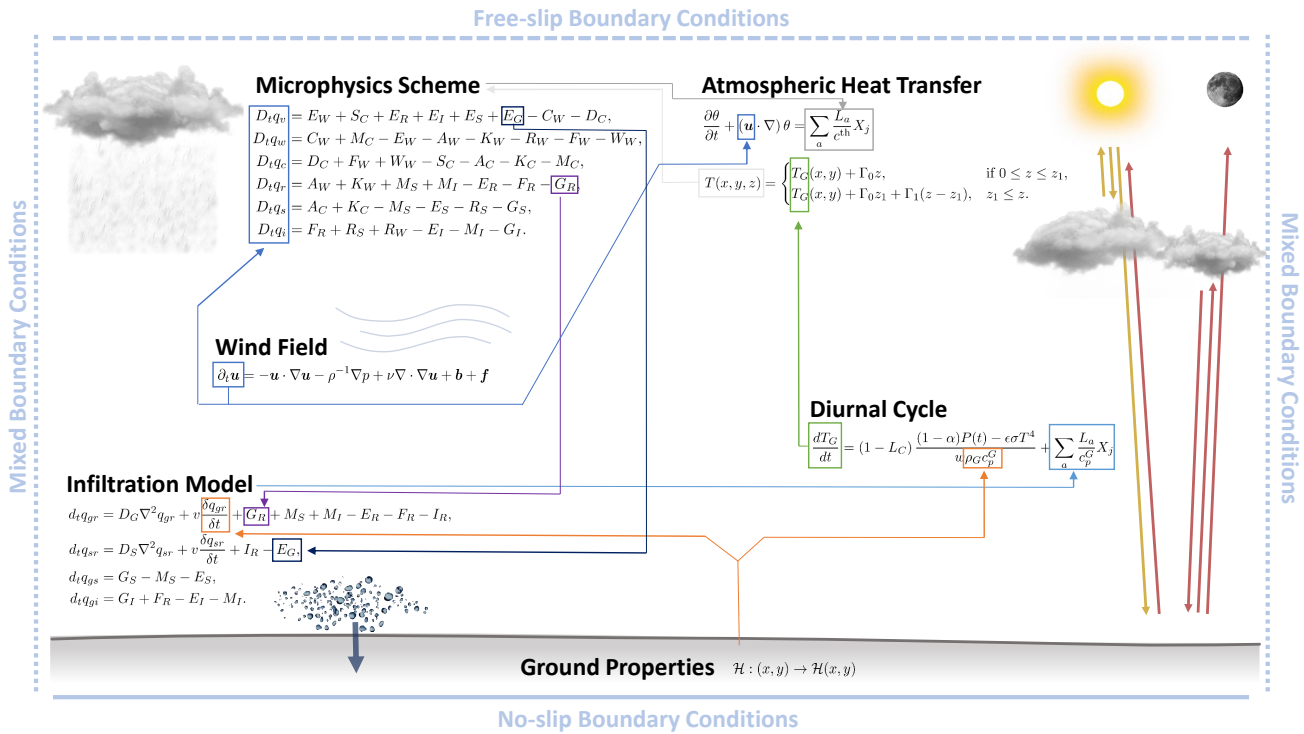


Fig. 3. Illustration of our microphysics scheme for modeling the water transport between different cloud and precipitation types.

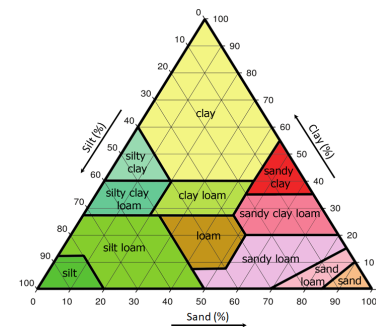
state of our ground system (which corresponds to water content at the ground  $q_{jg}$ , temperature  $T_C$  and cloud covering fraction  $L_C$ ). We include a variety of different landscape geometries by introducing a height map  $\mathcal{H} : (x, y) \rightarrow \mathcal{H}(x, y)$  such that the 2D ground grid will be embedded in 3D space as  $\partial\Omega_{\text{bottom}} = (x, y, \mathcal{H}(x, y))^T \in \Omega$ . The procedure summarized in Algorithm 1 starts by updating solar radiation using (59). Then, it updates ground conditions. Cloud covering is updated on each cell according to (60). After that, it computes ground temperature evolution caused by the diurnal cycle according to (63). Then water quantities  $q_{jg}$  are advected and diffused on the 2D grid, and their microphysics updated afterwards, following (52)–(55) with boundary conditions  $q_j = 0$  at the walls of the domain. Finally, heat transfer due to phase transitions at ground level is computed following (58). Atmospheric conditions are then updated. First, atmospheric temperature is computed following (1). Then, atmospheric water content  $q_j$ , potential temperature  $\theta$  and velocity field  $\mathbf{u}$  are advected, diffused, and pressure projected following the Eulerian fluid solver of Hädrić et al. [2020]. Next, we apply water content transfer from the atmosphere to the ground for precipitation types that have reached  $\partial\Omega_{\text{bottom}}$  by adding the atmospheric quantity  $q_j$  to its ground analogous to  $q_{jg}$ . Additionally, vorticity confinement is included as introduced by Steinhoff and Underhill [1994] to avoid nonphysical damping caused by numerical dissipation. Finally, the microphysics of the atmospheric water content is computed using (9)–(14), as well as the corresponding heat transfer due to phase transitions as described by (67). We apply no-slip boundary conditions at the ground, free-slip boundary

conditions at the top, and mixed boundary conditions at the sides: pure Neumann boundary conditions for  $\mathbf{u}$  and  $\theta$  are set to ambient temperature, periodic boundary conditions for  $q_v$ , and  $q_j$  are set identically to zero for all cloud and precipitation species.

## 5.2 Ground Parametrization

In order to include a variety of soil types while reducing the number of parameters that need to be set as an input in our solver, we employ a ground parametrization based on the United States Department of Agriculture (USDA) soil texture classification used in agriculture and soil sciences [Shirazi et al. 1988]. This is illustrated on the left.

Every ground property  $P$  used in our model (hydraulic conductivity  $\kappa$ , weighted diffusivity  $\bar{D}$ , evaporative ground coefficient  $\phi$ , heat capacity  $c_p^G$ , albedo  $\alpha$ , emissivity  $\epsilon$ , and density  $\rho_G$ ) is computed as a linear combination of the soil composition so that  $P = \gamma_1 P_{\text{sand}} + \gamma_2 P_{\text{silt}} + \gamma_3 P_{\text{clay}}$ , where each  $\gamma$  parameter indicates the corresponding material percentage (sand, silt and clay, correspondingly) with  $\gamma_1 + \gamma_2 + \gamma_3 = 1$ . We take the values of each  $P_{\text{sand}}$ ,  $P_{\text{silt}}$ , and  $P_{\text{clay}}$  from the literature [Groenendyk et al. 2015; Jury and Horton 2004; Nemes and Rawls 2004].



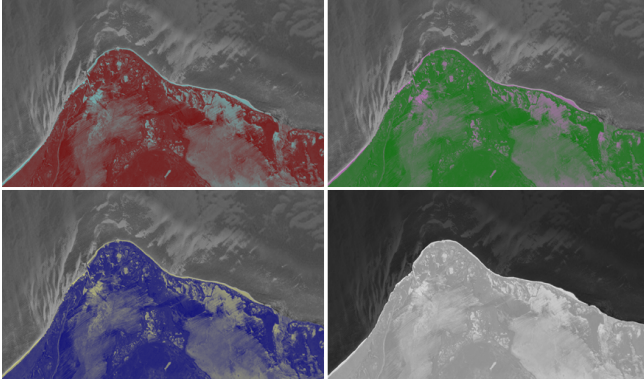


Fig. 4. Visualization of the material maps used for simulating the diurnal cycle on the coast of Yucatan (see Figure 15, top) with the corresponding satellite image in the background. These maps contain gamma values that correspond to the percentages of salt (red map), slit (green map), and clay (blue map) in the soil. The fourth map (white) is a binary function to distinguish between soil and oceanic water.

Additionally, we include terrains with oceanic water (see Figure 15, top) by considering the ocean part of  $\partial\Omega$  as a source of surface water with constant evaporation rate  $E_{\text{ocean}}$ . Plausible values for  $E_{\text{ocean}}$  were obtained from the literature [Yu 2007], while heat capacity, albedo, emissivity, and density are taken as those of water. Complex terrains with different ground compositions are parametrized using three material maps  $\mathcal{M}_i(x, y) \in [0, 1]$  that correspond to their gamma values, as well as a binary map  $\mathcal{M}_4(x, y) \in \{0, 1\}$  for distinguishing soil and oceanic water (Figure 4). Finally, following Hädrich et al. [2020], we simulate inhomogeneities in the initial distribution of  $q_{sr}$  using Perlin noise [1985] by introducing a noise map  $\mathcal{N}(x, y) \in [0, 1]$  with scaling parameter  $\gamma_{\text{Perlin}}$  so that, given an initial average subsurface water content  $\bar{q}_{sr}$ , local water content will be distributed as  $q_{sr}(x, y) = (\gamma_{\text{Perlin}}[2\mathcal{N}(x, y) - 1] + 1)\bar{q}_{sr}$ . Using this ground parametrization, we reduce our main parameter set to seven quantities: initial ground temperature  $T_G$ , initial average water content  $\bar{q}_{sr}$ , average solar irradiance  $\bar{P}$ , and material gamma factors  $\gamma_1, \gamma_2, \gamma_3$ , and  $\gamma_{\text{Perlin}}$ . Varying this canonical parameter set allows to simulate diverse weather phenomena on different terrains types (Figure 15) as well as local weather variations on a fixed terrain (Figure 1). A parameter set exploration is presented in Appendix C.

### 5.3 Implementation

We implemented Algorithm 1 within a C++/CUDA framework. We employ regular forward finite differences when updating water content and temperature at atmosphere and ground levels. Moreover, Hädrich et al. [2020] kindly provided the source code of their cloud simulator, which we extended by implementing our water continuity microphysics scheme for extended cloud and precipitation types, two-way coupling between ground and atmosphere with the corresponding heat transfer, and the role of the diurnal cycle in local weather evolution.

Table 1. Overview of the low-dimensional parameter set used in the scenes presented in this paper. Moreover, resolution (R) and computation time (T) measured in seconds per frame are listed. For all scenes, a constant time step size of  $\Delta t = 5$  min is used. Parameters are listed in  $[T_G] = 1^\circ \text{C}$ ,  $[q_{sr}] = 1 \text{ kg kg}^{-1}$ , and  $[\bar{P}] = 1 \text{ W m}^{-2}$ . Identical parameter values  $D_G = 1$ ,  $D_S = 0.001$ ,  $\Gamma = -6.5 \text{ K/km}$ , and  $z_1 = 8 \text{ km}$  are used in all simulations.

Fig.	Scene	$T_G$	$\bar{q}_{sr}$	$\bar{P}$	$\gamma_1$	$\gamma_2$	$\gamma_3$	$\gamma_{\text{Perlin}}$	R	T
5	Cumulo Comp.	21	0.82	-	-	-	-	0.02	$128 \times 128 \times 328$	0.12
6	H.P. Cumulonimbus	21	0.82	-	-	-	-	0.02	$328 \times 128 \times 328$	0.12
8	Multi-Layered	19	0.53	214.2	0.36	0.44	0.20	0.10	$228 \times 128 \times 228$	0.03
8	Mammatus	6	0.95	-	-	-	-	-	$228^3$	0.11
8	Hole-Punch	14	0.42	-	-	-	-	0.01	$128^3$	0.04
10	Light Rain	12	0.46	170.4	0.36	0.44	0.20	0.05	$228 \times 64 \times 228$	0.15
10	Heavy Rain	18	0.63	228.5	0.40	0.38	0.22	0.02	$228 \times 50 \times 228$	0.15
10	Hail Storm	-8	0.75	130.4	0.25	0.65	0.10	0.03	$228 \times 64 \times 80$	0.16
10	Snow Storm	-15	0.73	155.2	0.50	0.28	0.22	0.07	$128^3$	0.15
12	Foehn Effect	21	0.56	168.7	0.40	0.27	0.33	0.06	$228 \times 128 \times 128$	0.11
14	Hydrologic Cycle	21	0.81	168.7	0.40	0.27	0.33	0.11	$328 \times 64 \times 128$	0.12
15	Coast of Yucatan	26	0.83	199.7	0.65	0.20	0.15	0.06	$228 \times 128 \times 128$	0.11
15	Sahara Desert	-4	0.06	278.9	1.00	0.00	0.00	0.05	$228 \times 128 \times 128$	0.15
15	Swiss Alps	7	0.73	134.1	0.40	0.40	0.20	0.05	$228 \times 128 \times 128$	0.17
17	Mapinguari Park	19	0.71	188.5	0.35	0.45	0.20	0.06	$228 \times 128 \times 228$	0.16

## 6 RESULTS

We present a variety of results simulated using our framework according to Algorithm 1 and implemented as described in the previous section. Table 1 provides an overview of the different scenes presented throughout this section including relevant parameters. Computation times listed in Table 1 are measured on an up-to-date desktop computer running our simulation framework on an NVIDIA® GeForce® GTX 2080 Ti. Most scenes can be simulated interactively. To render these scenes, we used volume ray casting [Pharr et al. 2016] and particle systems within OpenGL/GLSL. Cloud volume and light interaction defines the final opacity and color for each pixel with cloud content, and particle systems allow to visualize different precipitation types depending on their average size and terminal velocity. The final results shown throughout this work are rendered offline using the Cycles renderer integrated in Blender.

### 6.1 Complex Cumulonimbus Clouds

Given their average height distributions, cumulonimbus usually start as warm clouds but, as they rise through the atmosphere and lose heat, transition to mixed-phase clouds and, finally, to cold clouds [Straka 2009]. Unlike Hädrich et al. [2020], who uses the classical Kessler model for parametrizing warm clouds only, we take into account these extra microphysical processes, which enables us to explore the impact of cloud glaciation on the formation and evolution of cumulonimbus. The heat released from vapor deposition and freezing of liquid water gives it an extra buoyancy force that allows it to reach higher altitudes as it glaciates at altitudes where  $T \leq -40^\circ \text{C}$ . In Figure 5 we compare the evolution of a high altitude cumulonimbus cloud simulated with the warm cloud Kessler model and with our microphysics scheme using the same initial and boundary conditions. Using the warm cloud model, the cumulonimbus does not rise to the altitude where it develops an anvil because, under this conditions ( $T \leq -40^\circ \text{C}$ ), it only has buoyancy due to vapor condensation at lower altitudes. Additionally, by including ice-phase precipitation types, we can model a high-precipitation cumulonimbus (Figure 6), in which a precipitation core (with snow, rain, and precipitated ice) is wrapped inside

the cloud matter content. In Figure 6 we show the anatomy of a high-precipitation cumulonimbus by separating its contents with color maps that show low amounts of precipitation in blue and high amounts of precipitation in purple. Moreover, in Figure 7 we plot the mixing ratio profiles of each precipitation and cloud types as a function of height in our cumulonimbus simulation. Mixing ratio at altitude  $h$  is computed as the average mixing ratio on the grid at  $z = h$ . Our profiles reflect the conditions of warm heavy rain [Song and Sohn 2018]. While there is snow within the cloud, it melts completely into rainwater before reaching the ground at 6.2 km. Precipitated ice also melts as it descends but it reaches lower altitudes (5.0 km) as it does not melt immediately. In the range from 7.8 km to 13.1 km, cumulonimbus is a mixed-phase cloud composed of both supercooled water and ice that has formed due to the WBF mechanism.

## 6.2 Ice-Phase Phenomena

Our framework is capable of simulating several complex physical phenomena caused by the interplay of different water phase transitions within clouds. In this section we present three cloud formations that form due to ice-phase effects.

**6.2.1 Hole-Punch Clouds.** As described in Section 4.2.2, at temperatures between  $-40^{\circ}\text{C}$  and  $0^{\circ}\text{C}$ , the water content of a cloud can continue in its liquid phase as supercooled water as long as it does not start nucleating around either an artificial (e.g. aerosol emission) or a natural particle via the WBF process. When the water within an altocumulus cloud is supercooled and there is a trigger for small nucleation (e.g. an airplane flying through the cloud), the WBF process causes a domino effect in the surrounding water droplets, which quickly evaporate and thus create a hole in the cloud with ice crystals inside it. This is called a fallstreak hole or hole-punch cloud because of the usually circular or elliptical gap in the cloud. We can reproduce this cloud as demonstrated in Figure 9 by applying our explicit parametrization of the WBF process in the vicinity of a simulated nucleation event. We first simulate the supercooled altocumulus and then apply the nucleation at a fixed position where the WBF process creates the warm cloud evaporation and subsequently the deposition into ice crystals that can be seen inside the hole-punch. We also show (Figure 8, c) hole-punch clouds generated using our framework and a photo comparison.

**6.2.2 Mammatus Clouds.** In its long-time evolution, the anvil of a cumulonimbus cloud gradually subsides as it spreads out from its source cloud. As air descends and warms, there will be a differential warming in the cloud layers that destabilizes it [Barry 1977]. Cooling due to latent heating effects of rain, snow, and graupel fallout contributes to further destabilization that results in convective overturn and creates a lumpy cloud-base known as mammatus cloud [Ley 1894]. Based on the detailed precipitation and temperature profiles measured by Trömel [2017], and Kanak and Straka [2006] for different mammatus clouds, we prescribed precipitation and atmospheric heat initial conditions to match the conditions in which these clouds form. In Figure 8 (b) we show the result of our mammatus simulation (left and middle) with a photo comparison (right). Please note that the precise physical mechanism for mammatus formation is still up

to debate [Ravichandran et al. 2020], yet our model captures this phenomenon if atmospheric conditions known to lead to mammatus clouds are prescribed.

**6.2.3 Multi-Layer Clouds.** Our infiltration and diurnal models coupled with the extended microphysics scheme allow to simulate the formation of multiple cloud types at different altitudes. Figure 8 (a) illustrates this multi-layer cloud formation with a view from the ground (left) and a view at cloud height (middle). At the beginning, surface water is evaporated by incoming solar radiation from the sun and this vapor is then deposited into cold cloud content. Later, when more vapor is available via ground evaporation of subsurface water and the diurnal cycle continues, new warm clouds emerge at lower altitudes.

## 6.3 Precipitation Types

As shown in Figure 10, our framework is capable of simulating different precipitation events, such as stratocumulus clouds generating light rain in the Appalachian Mountains (a), heavy rain in Blue Ridge Mountains (b), a winter storm in the vicinity of the Popocatepetl Volcano (c), and heavy snowfall in the Yosemite National Park (d). Rain, snow, and precipitated ice are formed as a consequence of the microphysical processes within cloud matter that are expressed in our model. Different cloud and precipitation types in these scenes are generated varying our main parameter set (Appendix C). Specifically, using a high ground temperature  $T_G$  and subsurface water content  $q_{sr}$  forms warm clouds, and decreasing the temperature while maintaining water content allows to create mixed-phase and cold clouds with their corresponding precipitation types. Furthermore, the amount of precipitation is controlled by changing initial water content  $q_{sr}$ . For in-scene visualizations, we measure average precipitation mixing ratios in each scene and then use the assumed size and terminal velocity distributions (Appendix B) to compute the average falling velocity and particle size for the particle system that represents each precipitation (see Figure 11).

## 6.4 Foehn Effect

Foehn winds are warm, dry downslope winds that occur on the lee side of a topographic barrier [Richner and Hächler 2013]. This phenomenon starts with the flow air that encounters a mountain barrier and is forced to ascend and cool. After crossing the mountains, the air flows down the slopes and warms adiabatically as it descends, creating a temperature gradient on the other side of the mountains. When the saturation vapor pressure is reached before the air crosses the mountains, its water vapor condenses into clouds and precipitation that lies over and along the mountain ridge but usually evaporates on the leeward slopes because humid air rising loses less temperature than dry air descending due to differences in heat capacity. These clouds are known as Foehn walls. We simulate the Foehn effect as shown in Figure 12 by applying a wind field on an already condensed warm air on one side of the mountain. Our atmospheric heat transfer model is able to reproduce Foehn wall clouds because the extra heat on the other side of the mountain dries and evaporates incoming clouds. Furthermore, the resulting temperature gradient is also captured by our model, as it can be seen in Figure 13.

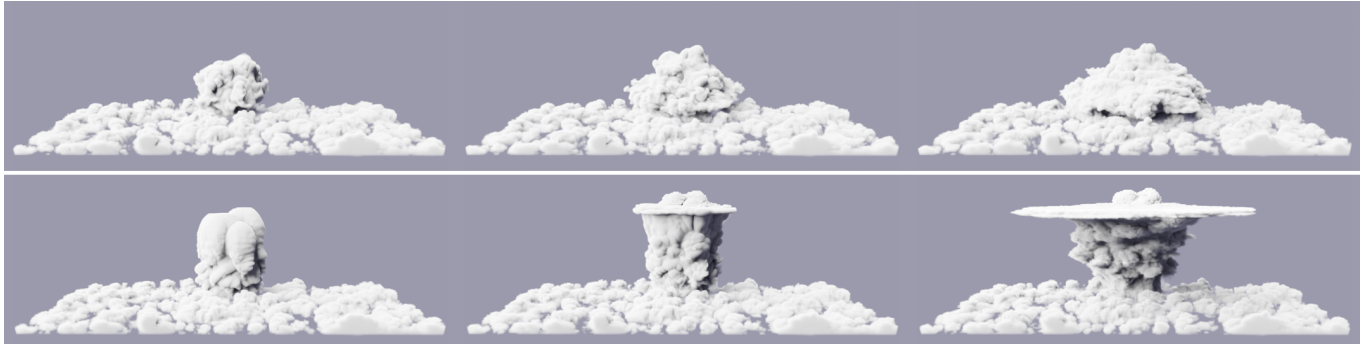


Fig. 5. Temporal evolution of a high altitude cumulonimbus cloud emerging from cumulus clouds generated with the classical Kessler model (top) and with our extended microphysics scheme (bot). The inclusion of ice-phase transitions and their corresponding thermodynamics gives the cloud an extra buoyancy that allows to more realistically simulate the formation of these types of clouds.

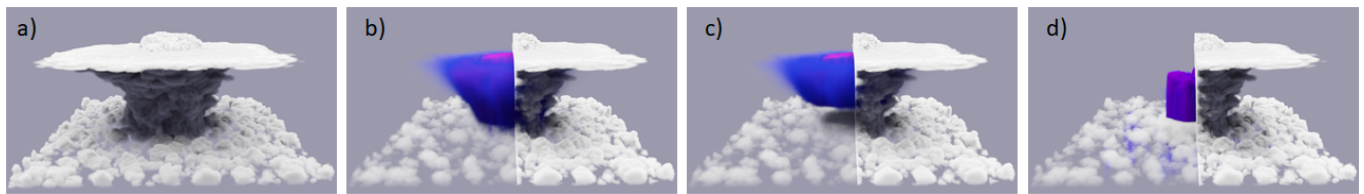


Fig. 6. High-precipitation cumulonimbus generated with our framework (a). We use a color map (from blue to purple) to visualize the amount of precipitation types, clouds have been removed from half of the scene for better visualization: (b) precipitated ice, (c) snow, and (d) rain.

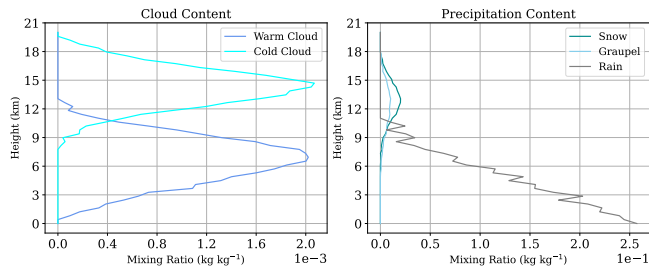


Fig. 7. Mixing ratio profiles for each cloud and precipitation type of a high precipitation cumulonimbus simulated with our framework.

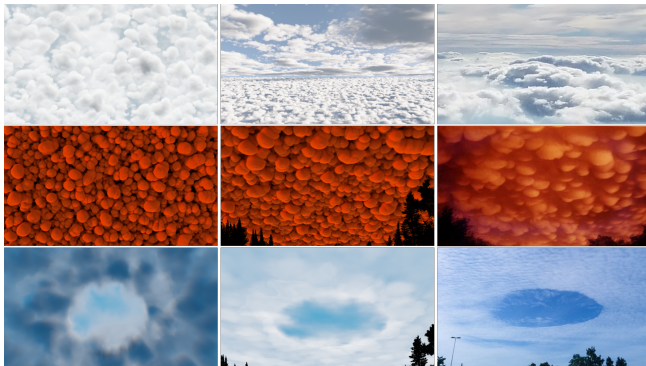


Fig. 8. Different ice-phase cloud formations (left and middle) with corresponding photo comparisons (right) : multi-layer clouds (top), mammatus (middle), and hole-punch (bottom).



Fig. 9. Temporal evolution of an altocumulus cloud made up of supercooled water transitioning into a hole-punch cloud due to sudden nucleation and the WBF process.

### 6.5 Hydrologic Cycle

Water is continuously moved in its different phases by means of the hydrologic cycle. This process involves the exchange of energy between ground, atmosphere and the sun, as well as the water changes on, above, and below the surface of the earth. To further showcase the capabilities of physically accurate cloud, ground, and atmospheric models, we reproduce the hydrologic cycle as demonstrated in Figure 14. We initialize our simulation with a storm on top of the mountains during the night. As in the high-precipitation cumulonimbus, cold precipitation is melt into rainwater that is transported down the mountains via surface and subsurface water content due to the geometry of the terrain. Then, as the sun emerges and atmospheric conditions change, rainfall ends. Afterwards, when the ground water is evaporated again to the atmosphere, stratus clouds form on the other parts of the terrain.

### 6.6 Weatherscapes

The two-way coupling of ground and atmosphere allows our model to simulate complex dynamic scenes under different weather conditions (Figure 15) such as a warm day at the coast of Yucatan, several

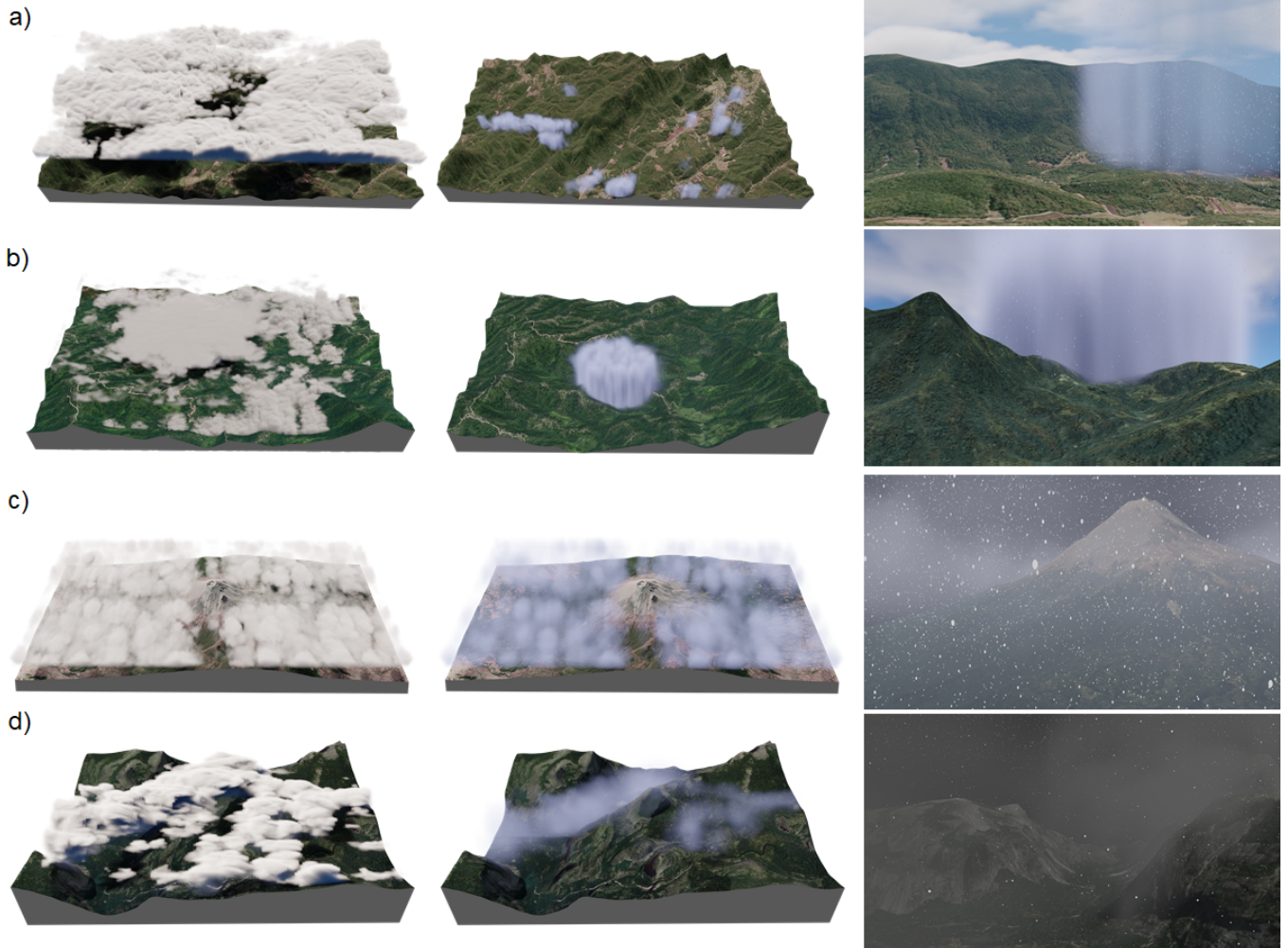


Fig. 10. Different precipitation events simulated using our framework. We can visualize clouds (left), precipitation amount (middle) and falling precipitation (right): a) Light rain in Appalachian Mountains, b) Heavy rain in Blue Ridge Mountains, c) Winter Storm in the Popocatepetl Volcano, and d) Heavy Snowfall in Yosemite National Park.

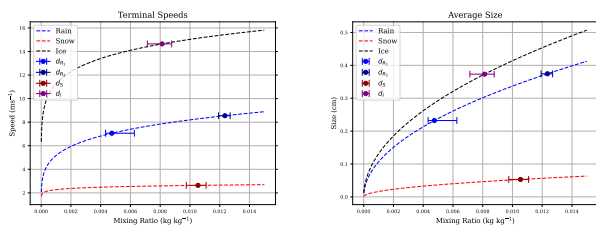


Fig. 11. Terminal speed and average size of each precipitation type as a function of its mixing ratio. The isolated points depict the average mixing ratio in each scene with the bars corresponding to the minimum and maximum values encountered in the simulation: light rain ( $d_{R_1}$ ), heavy rain ( $d_{R_2}$ ), snow storm ( $d_S$ ), and precipitated ice storm ( $d_I$ ).

cloud formations over the Swiss Alps, and the extreme temperature variations in the Sahara desert. In the Yucatan coast scene we employ a material map as shown in Figure 4 to distinguish from the sandy loam terrain of the beach and the surrounding water. We start the scene with a small cloud formation around the coast that develops further due to water evaporation. In the night, when water has been evaporated from the ground, clouds emerge also on the beach. For the Swiss Alps we use a loam parametrization for the terrain and start with small clouds that develop throughout the diurnal cycle. In the Sahara desert scene we employ a sandy terrain and start with no clouds but with liquid content as subsurface water in the ground. For all the simulations, we set up the initial ground temperature and incoming solar radiation based on real data from weather services as described in Section 6.7. Additionally, we measure the average temperature  $T_G$  and cloud covering evolution on each scene, as can be seen in Figure 16. Temperature oscillations on both the coast

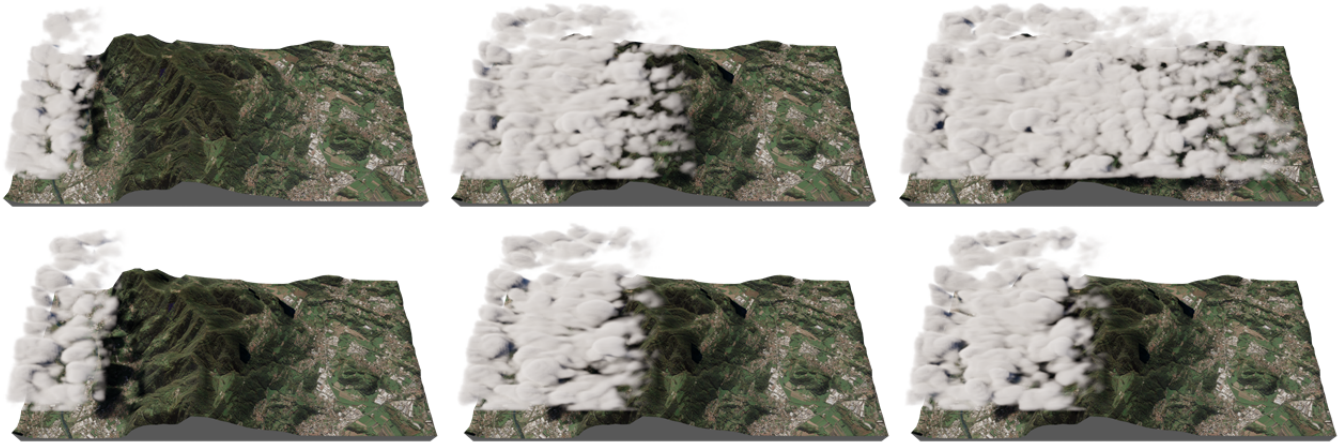


Fig. 12. Evolution of cloud formations passing by a topographic barrier without atmospheric heat transfer (top) and with atmospheric heat transfer (bottom). The inclusion of heat transfer in the atmosphere allows us to recreate the Foehn effect. The resulting temperature gradient blocks incoming clouds and results in a Foehn wall.

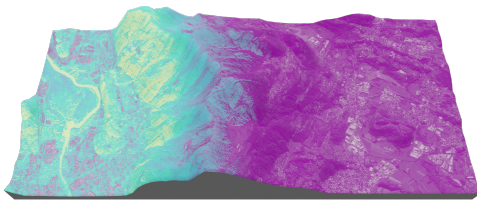


Fig. 13. Colormap visualization (blue to purple, as temperature increases) of the temperature profile  $T_G(x, y)$  under the Foehn effect discussed in Figure 12. Incoming wind (from left to right) approaches a topographical barrier. The interaction between wind and the mountain terrain geometry creates differential temperature gradient.

and the mountain scenes present a small variance as the diurnal cycle evolves due to their terrain properties that allow them to sustain a cloudy environment (cloud coverage preserves heat by reflecting both solar and infrared radiation). This correctly reflects temperature behaviour on such weather conditions [Ahrens 2014]. On the other hand, the drier sandy terrain in the Sahara desert does not create many clouds, which rapidly increases its temperature during the day as incoming solar radiation heats the ground, and analogously decreases it at night when infrared radiation takes heat out of the ground into space. This results on extreme temperature variations, which also coincides with the expected behaviour in such environments [Ahrens and Henson 2021].

## 6.7 Weather Nowcasting

To assess the prediction capabilities of our atmospheric, ground and microphysics schemes, we coupled our framework with sun angle, irradiance and atmospheric measurements of weather services to

simulate the diurnal cycle and cloud formation interactively, enabling weather nowcasting. After manually selecting a geographic location, we obtain the day duration, sunrise hour and average solar irradiance in the area as well as temperature, humidity, and wind maps by different weather services<sup>2,3,4</sup>. Following Hädrich et al. [2020], we approximate the wind field by tracking the motion of streamlines with optical flow [Itseez 2015] and interpolating the resulting motion vectors to sample wind speeds. However, in our model we take weather input data as initial conditions only and then let the system evolve over the diurnal cycle, which allows for a combination of nowcasting and forecasting. In Figure 17 we present the result of weather nowcasting for the Matinguari National Park in Brazil on March 26, 2021 at 3am local time and its temporal evolution through the diurnal cycle. Moreover, we compute the average temperature at ground level, relative humidity at  $z = 1$  km, and cloud covering in our simulation and compare them to the weather service measurements to quantitatively assess our model. The results are shown in Figure 18. The overall temperature, humidity, and cloud covering dynamics are captured correctly by our simulation, with errors introduced mainly because we do not consider the effect of incoming clouds from neighboring regions due to local winds, which would otherwise change the cloud covering (bottom right plot), and more precisely describe the diurnal cycle. This strong winds scenario represents an extreme case that challenges our model. It could, however, be solved by having dynamic boundary conditions to handle incoming clouds and thus a more complex cloud covering. In Figure 18 we also compute the normalized radiation intensity for both infrared and solar radiation. Our model reproduces the common lag between maximum solar radiation and maximum daily temperature [Ahrens and Henson 2021]. Even after solar radiation has reached its maximum intensity, the

<sup>2</sup><https://globalsolaratlas.info>

<sup>3</sup><https://www.ventusky.com>

<sup>4</sup><https://www.timeanddate.com>

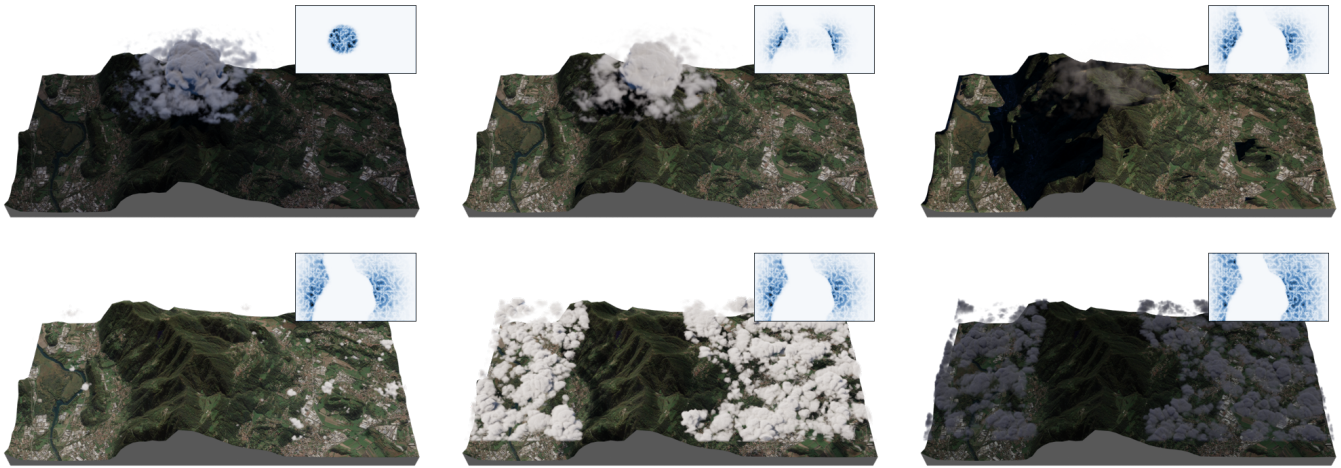


Fig. 14. Temporal evolution (left to right, top to bottom) of our simulation of the hydrologic cycle. Each image also shows its corresponding subsurface water content. A heavy storm generates rainwater that is transported down the mountains. As day progresses, this water content in the ground is evaporated back to the atmosphere and condenses back into clouds.

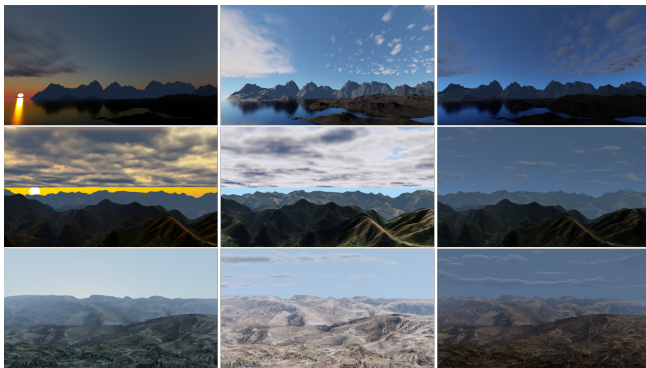


Fig. 15. Simulations of different weatherscapes using our framework. A heavy cloudy morning in the coast of Yucatan, Mexico (top scene) develops during the day (middle) resulting in a warm cloudy night in the land (right). In the Alps (middle scene), different cloud patterns develop from the morning until the night. The dry Sahara Desert (bottom scene) does not have enough vapor content to create clouds, which results in a very hot temperature during the day as there is no covering from incoming solar radiation. After subsurface water has evaporated, small clouds appear at the afternoon (middle) and continue developing during the night (right).

energy surplus still exceeds outgoing heat from infrared radiation after a couple of hours, which causes the maximum temperature of the day to delay until infrared radiation exceeds the energy surplus and temperature starts decreasing during the night.

## 7 EVALUATION

Qualitatively, our model is validated by reproducing cloud formations that form due to the complex interplay of ground, atmosphere and water content in the form of vapor, ice, and liquid water. This is illustrated in Figure 8 where we reproduce three mixed-phase

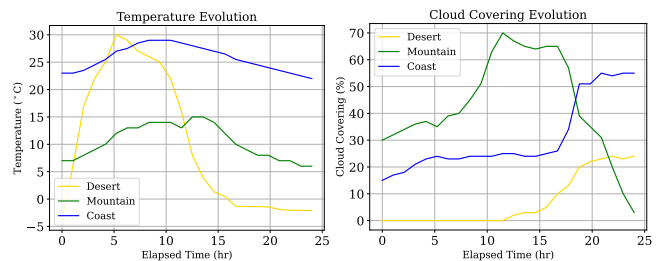


Fig. 16. Ground temperature and cloud covering time evolution in the different weatherscapes showed in Figure 15. Ground composition and cloud coverage allow the coast and mountain environments to develop a small variance in their temperature throughout the diurnal cycle. Desert, on the other hand, presents extreme temperature changes due to its soil properties (pure sand) and its lack of a cloud cover that reflects solar radiation during the day and retains infrared radiation during the night.

cloud phenomena. Our ground infiltration/evaporation model allows us to model multi-layer clouds. The explicit parametrization of the WBF process enables us to reproduce the transition of a super-cooled cloud to punch-hole formations, and including cold, warm, and mixed cloud and precipitation types and their interactions let us form mammatus clouds by prescribing atmospheric conditions based on precipitation and temperature profiles observed during mammatus events. Additionally, our integrated model is assessed visually in Figures 10 and 15, where we create different precipitation events and weather environments by adjusting ground properties and atmospheric conditions, as well as in Figure 14, where we simulate the hydrologic cycle: snow from a storm melts into rainwater that is transported down the mountains and then evaporates again during the day and forms stratus clouds. Moreover, in Figure 5 we compare our framework to a state-of-the-art cloud simulator [Hädrich et al. 2020]. Our extended model improves the physical



Fig. 17. Simulation of the diurnal cycle evolution (from top to bottom, left to right) at Mapinguari National Park on March 26, 2021, starting at 3am local time. We use weather data streamed to our framework as input initial conditions.

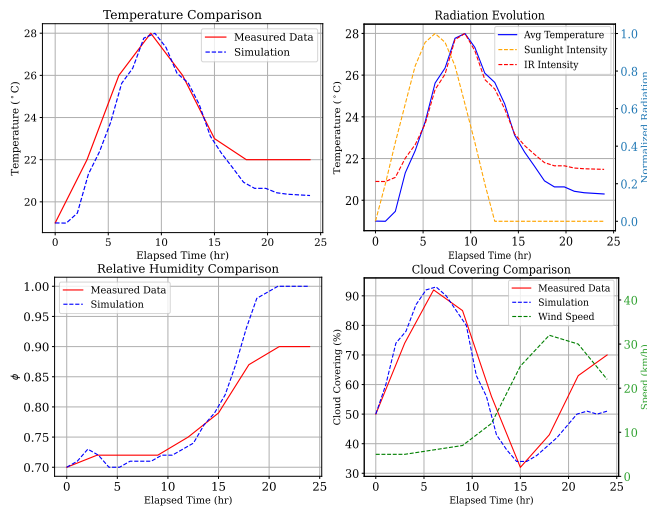


Fig. 18. Temporal evolution of diverse weather parameters in our simulation of the diurnal cycle at Mapinguari National Park. We compare our results with measurements from weather services in terms of temperature (top left), relative humidity (bottom left), and cloud covering (bottom right). Our model captures the overall behaviour of the diurnal cycle. Additionally, the evolution of solar and IR radiation intensities (top right) show that our simulation reproduces the common lag between maximum solar radiation and maximum daily temperature.

behaviour of cumulonimbus clouds. Finally, in Figures 12 and 13 we validate our atmospheric heat transfer model by simulating the Foehn effect, where we capture both Foehn walls and the ground temperature gradient generated by this effect. Quantitatively, we evaluate our model creating a high-precipitation cumulonimbus by prescribing atmospheric conditions based on infrared satellite

observations [Blyth et al. 2015]. Our measured mixing ratio profiles (Figure 7) reflect the conditions of warm heavy rain [Song and Sohn 2018], where there is a precipitation core wrapped inside the cloud content. In this type of storm, precipitated ice and snow are present in the atmosphere but melt before reaching the ground. Moreover, our cumulonimbus reproduces the transition from warm cloud ( $h \leq 7.8$  km) to mixed-phase cloud ( $7.8 \text{ km} \leq h \leq 13.1$  km) and, finally, to cold cloud ( $h \geq 13.1$  km) due to the extensive height of this type of cloud. Additionally, we compute the temperature evolution (Figure 16) of the three different environments that we simulated: coast of Yucatan, Swiss Alps, and Sahara Desert. Our results reflect the warm temperatures of Yucatan and Sahara as well as the colder Alps. Moreover, while the sandy loam terrain in Yucatan and loam ground of the Alps is capable of sustaining a cloudy environment (and thus prevent temperature from changing drastically as clouds act as a cover that reflects solar and infrared radiation), the drier sandy terrain in the Sahara desert does not create many clouds, which causes the temperature to drastically change from day to night as there is almost no cloud covering. Finally, we validate our model by streaming weather data to our framework as initial conditions for our simulations. Temperature evolution in our implementation of the diurnal cycle at the Mapinguari National Park (Figure 18) captures the behaviour of measured data from weather services, as well as the common lag between maximum solar radiation and maximum daily temperature.

## 8 DISCUSSION AND LIMITATIONS

Our physics-based model for weather simulation enables the realistic simulation of different weatherscapes and complex phenomena at ground and atmospheric levels. By parametrizing the underlying physical processes in weather dynamics, we are able to capture the interplay of water transport in its different phases at atmospheric, ground and subground layers, the diurnal cycle fueled by incoming solar radiation and outgoing infrared radiation, and atmospheric

changes due to wind fields and atmospheric heat transfer. This enables us to simulate mixed-phase cloud formations such as mammatus, multi-layer, and hole-punch clouds, as well as reproducing different weatherscapes such as cold mountains, warm coasts and the extreme conditions encountered in deserts. Furthermore, our method captures the emergent dynamics of the diurnal cycle, which can be coupled with weather data for enabling nowcasting in real-time and local forecasting. In an extension of Hädrich et al. [2020], we reformulate the microphysics parametrization of atmospheric and ground water content to include different cloud and precipitation types, and also express the feedback between clouds, atmosphere and ground properties. As discussed in Section 6.7, when streaming weather data to our framework for local forecasting, our model deviates from measured data as time passes since we do not take into account weather variations in the vicinity of our simulated region, such as incoming warm/cold fronts or clouds that are transported into the region of interest and thus changing water content and cloud coverage. This phenomena could be included, for example, by implementing more complex dynamic boundary conditions. Moreover, changing boundary conditions dynamically (particularly, incoming solar radiation and water content) could also be applied to simulate local weather changes that mimic the seasonal cycle. Another process that is not included in our model is ground and vegetation feedback, specifically through evapotranspiration. This would allow us to explore more complex biomes and their role in changing weather conditions. Finally, our diurnal cycle temperature model can be improved by considering a dynamic albedo that is influenced by both deposited snow and vegetation content in the terrain, as well as ground diffusion and convection heat dynamics.

## 9 CONCLUSION AND FUTURE WORK

We have presented a novel physics-based model for weather simulation. Our approach models and integrates atmospheric and ground processes by using explicit parametrizations of the underlying fluid dynamics, heat dynamics, and microphysics processes that cause local weather changes. This enables the exploration of realistic and large-scale weatherscapes. We have shown that our framework can capture different types of weather phenomena like the Foehn effect and the hydrologic cycle, as well as mixed-phase cloud formations like mammatus, hole-punch, and multi-layered clouds. Furthermore, we have streamed weather data to our model to simulate realistic weatherscapes under very different ground and atmospheric conditions, and have assessed quantitatively the prediction capabilities of our scheme by comparing our results to weather data.

Future work in this direction includes exploring vegetation feedback, a dynamic albedo, and more complex ground heat transfer, all of which could open the possibility to explore more varied weatherscapes. Moreover, it would be interesting to dynamically change boundary conditions to model the interaction of the local region with its surroundings and weather changes that are caused by non-local phenomena such as seasonal changes. Finally, while our framework allows to explore weatherscapes interactively, execution time and resolution could be improved by using an adaptive grid technique.

## ACKNOWLEDGMENTS

This work was supported and funded by KAUST through the baseline funding of the Computational Sciences Group within the Visual Computing Center. The insightful discussions with Miłosz Makowski and Weronika Skowrońska as well as the reviewers' valuable comments that improved the manuscript are gratefully acknowledged.

## REFERENCES

- C. D. Ahrens. 2014. *Essentials of meteorology: an invitation to the atmosphere*. Cengage Learning.
- C. D. Ahrens and R. Henson. 2021. *Meteorology today: an introduction to weather, climate, and the environment*. Cengage learning.
- O. A. Alduchov and R. E. Eskridge. 1996. Improved Magnus form approximation of saturation vapor pressure. *Journal of Applied Meteorology and Climatology* 35, 4 (1996), 601–609.
- J. D. Anderson. 2003. *Modern compressible flow*. Tata McGraw-Hill Education.
- Standard Atmosphere. 1975. International organization for standardization. *ISO 2533* (1975), 1975.
- A. H. Auer. 1972. Distribution of graupel and hail with size. *Monthly Weather Review* 100, 5 (1972), 325–328.
- R. G. Barry. 1977. *International Cloud Atlas, Volume I: Manual on the Observation of Clouds and Other Meteors*.
- A. M. Blyth, L. J. Bennett, and C. G. Collier. 2015. High-resolution observations of precipitation from cumulonimbus clouds. *Meteorological applications* 22, 1 (2015), 75–89.
- A. Bouthors and F. Neyret. 2004. Modeling clouds shape. In *Eurographics 2004 - Short Presentations*, M. Alexa and E. Galin (Eds.). Eurographics Association.
- R. Bridson. 2015. *Fluid Simulation for Computer Graphics*. CRC Press.
- R. Bridson and M. Müller-Fischer. 2007. Fluid simulation: SIGGRAPH 2007 Course Notes. (08 2007), 1–81.
- W. Brutsaert. 2014. Daily evaporation from drying soil: Universal parameterization with similarity. *Water Resources Research* 50, 4 (2014), 3206–3215.
- A. Chern, F. Knöppel, U. Pinkall, P. Schröder, and S. Weißmann. 2016. SchröDinger's Smoke. *ACM Trans. Graph.* 35, 4, Article 77 (July 2016), 13 pages.
- W. R. Cotton. 1972. Numerical simulation of precipitation development in supercooled cumuli—Part II. *Monthly Weather Review* 100, 11 (1972), 764–784.
- F. Da, D. Hahn, C. Batty, C. Wojtan, and E. Grinspun. 2016. Surface-Only Liquids. *ACM Trans. on Graphics (SIGGRAPH 2016)* (2016).
- Y. Dobashi, K. Kusumoto, T. Nishita, and T. Yamamoto. 2008. Feedback Control of Cumuliform Cloud Formation Based on Computational Fluid Dynamics. In *ACM SIGGRAPH 2008 Papers (SIGGRAPH '08)*. Association for Computing Machinery, Article Article 94, 8 pages.
- J. Dudhia. 1989. Numerical study of convection observed during the winter monsoon experiment using a mesoscale two-dimensional model. *Journal of Atmospheric Sciences* 46, 20 (1989), 3077–3107.
- A. Voldoire et al. 2013a. The CNRM-CM5.1 global climate model: description and basic evaluation. *Climate dynamics* 40, 9 (2013), 2091–2121.
- B. Stevens et al. 2013b. Atmospheric component of the MPI-M Earth system model: ECHAM6. *Journal of Advances in Modeling Earth Systems* 5, 2 (2013), 146–172.
- F. Hourdin et al. 2013c. LMDZ5B: the atmospheric component of the IPSL climate model with revisited parameterizations for clouds and convection. *Climate Dynamics* 40, 9–10 (2013), 2193–2222.
- J. H. Van Boxel et al. 1997. Numerical model for the fall speed of rain drops in a rain fall simulator. In *Workshop on wind and water erosion*. 77–85.
- R. L. Miller et al. 2006. Mineral dust aerosols in the NASA Goddard Institute for Space Sciences ModelE atmospheric general circulation model. *Journal of Geophysical Research: Atmospheres* 111, D6 (2006).
- S. Watanabe et al. 2011. MIROC-ESM 2010: Model description and basic results of CMIP5-20c3m experiments. *Geoscientific Model Development* 4, 4 (2011), 845–872.
- C. W. Ferreira Barbosa, Y. Dobashi, and T. Yamamoto. 2015. Adaptive Cloud Simulation Using Position Based Fluids. *Comput. Animat. Virtual Worlds* 26, 3–4 (2015), 367–375.
- N. H. Fletcher. 2011. *The physics of rainclouds*. Cambridge University Press.
- I. Garcia-Dorado, D. G. Aliaga, S. Bhalachandran, P. Schmid, and D. Niyogi. 2017. Fast Weather Simulation for Inverse Procedural Design of 3D Urban Models. *ACM Trans. Graph.* 36, 2, Article Article 21 (2017), 19 pages.
- G. Y. Gardner. 1985. Visual Simulation of Clouds. In *Proceedings of the 12th Annual Conference on Computer Graphics and Interactive Techniques (SIGGRAPH '85)*. Association for Computing Machinery, 297–304.
- C. Gissler, A. Henne, S. Band, A. Peer, and M. Teschner. 2020. An Implicit Compressible SPH Solver for Snow Simulation. *ACM Trans. Graph.* 39, 4, Article 36 (July 2020), 16 pages.

- P. Goswami and F. Neyret. 2017. Real-Time Landscape-Size Convective Clouds Simulation and Rendering. In *Proceedings of the 13th Workshop on Virtual Reality Interactions and Physical Simulations (VRIPHYS '17)*. Eurographics Association, 1–8.
- E. J. Griffith, F. H. Post, T. Heus, and H. J. J. Jonker. 2009. *Interactive simulation and visualisation of atmospheric large-eddy simulations*. Technical Report. Technical Report 2 TuDelft Data Visualization Group.
- D. G. Groenendyk, T. P. A. Ferré, K. R. Thorp, and A. K. Rice. 2015. Hydrologic-process-based soil texture classifications for improved visualization of landscape function. *PLoS one* 10, 6 (2015), e0131299.
- K. L. S. Gunn and J. S. Marshall. 1958. The distribution with size of aggregate snowflakes. *Journal of Atmospheric Sciences* 15, 5 (1958), 452–461.
- T. Hädrich, D. T. Banuti, W. Palubicki, S. Pirk, and D. L. Michels. 2021. Fire in Paradise: Mesoscale Simulation of Wildfires. *ACM Transaction on Graphics* 40, 4, Article 163 (08 2021).
- T. Hädrich, M. Makowski, W. Palubicki, D. T. Banuti, S. Pirk, and D. L. Michels. 2020. Stormscapes: Simulating Cloud Dynamics in the Now. *ACM Transaction on Graphics* 39, 6, Article 175 (12 2020).
- M. J. Harris, W. V. Baxter, T. Scheuermann, and A. Lastra. 2003. Simulation of Cloud Dynamics on Graphics Hardware. In *ACM SIGGRAPH/EUROGRAPHICS Conference on Graphics Hardware (HWS '03)*. Eurographics Association, 92–101.
- S.-Y. Hong, J. Dudhia, and S.-H. Chen. 2004. A revised approach to ice microphysical processes for the bulk parameterization of clouds and precipitation. *Monthly weather review* 132, 1 (2004), 103–120.
- R. E. Horton. 1941. An approach toward a physical interpretation of infiltration-capacity. *Soil science society of America journal* 5, C (1941), 399–417.
- R. A. Houze. 2014. *Cloud Dynamics*. Elsevier.
- E.-Y. Hsie, R. D. Farley, and H. D. Orville. 1980. Numerical simulation of ice-phase convective cloud seeding. *Journal of Applied Meteorology and Climatology* 19, 8 (1980), 950–977.
- L. Huang, T. Hädrich, and D. L. Michels. 2019. On the Accurate Large-Scale Simulation of Ferrofluids. *ACM Trans. Graph.* 38, 4, Article 93 (July 2019), 15 pages.
- L. Huang and D. L. Michels. 2020. Surface-Only Ferrofluids. *ACM Trans. Graph.* 39, 6, Article 174 (Nov. 2020), 17 pages.
- G. Itseez. 2015. Open source computer vision library.
- W. A. Jury and R. Horton. 2004. *Soil physics*. John Wiley & Sons.
- J. T. Kajiya and B. P. Von Herzen. 1984. Ray Tracing Volume Densities. *SIGGRAPH Comput. Graph.* 18, 3 (1984), 165–174.
- K. M. Kanak and J. M. Straka. 2006. An idealized numerical simulation of mammatus-like clouds. *Atmospheric Science Letters* 7, 1 (2006), 2–8.
- B. Kärcher and U. Burkhardt. 2008. A cirrus cloud scheme for general circulation models. *Quarterly Journal of the Royal Meteorological Society* 134, 635 (2008), 1439–1461.
- E. Kessler. 1995. On the continuity and distribution of water substance in atmospheric circulations. *Atmospheric Research* 38, 1 (1995), 109–145.
- B. Kim, V. C. Azevedo, M. Gross, and B. Solenthaler. 2020. Lagrangian Neural Style Transfer for Fluids. *ACM Transaction on Graphics (SIGGRAPH)* (2020).
- T. Kim and M. C. Lin. 2003. Visual simulation of ice crystal growth. In *Proceedings of the 2003 ACM SIGGRAPH/Eurographics symposium on Computer animation*. Citeseer, 86–97.
- D. Koschier, J. Bender, B. Solenthaler, and M. Teschner. 2019. Smoothed Particle Hydrodynamics Techniques for the Physics Based Simulation of Fluids and Solids. In *Eurographics 2019 - Tutorials*, W. Jakob and E. Puppo (Eds.). The Eurographics Association.
- P. K. Kundu, I. M. Cohen, and D. R. Dowling. 2012. *Fluid mechanics*, 5th version. Academic, Berlin (2012).
- R. Lal and M. K. Shukla. 2004. *Principles of soil physics*. CRC Press.
- W. C. Ley. 1894. *Cloudland: A study on the structure and characters of clouds*. E. Stanford.
- Z. Li, H. W. Barker, and L. Moreau. 1995. The variable effect of clouds on atmospheric absorption of solar radiation. *Nature* 376, 6540 (1995), 486–490.
- Y.-L. Lin, R. D. Farley, and H. D. Orville. 1983. Bulk parameterization of the snow field in a cloud model. *Journal of Applied Meteorology and climatology* 22, 6 (1983), 1065–1092.
- J. D. Locatelli and P. V. Hobbs. 1974. Fall speeds and masses of solid precipitation particles. *Journal of Geophysical Research* 79, 15 (1974), 2185–2197.
- D. Lubin, J.-P. Chen, P. Pilewskie, V. Ramanathan, and F. Valero. 1996. Microphysical examination of excess cloud absorption in the tropical atmosphere. *Journal of Geophysical Research: Atmospheres* 101, D12 (1996), 16961–16972.
- M. P. Meyers, P. J. DeMott, and W. R. Cotton. 1992. New primary ice-nucleation parameterizations in an explicit cloud model. *Journal of Applied Meteorology and Climatology* 31, 7 (1992), 708–721.
- R. Miyazaki, Y. Dobashi, and T. Nishita. 2002. Simulation of Cumuliform Clouds Based on Computational Fluid Dynamics. In *Eurographics*.
- H. Morrison, J. A. Milbrandt, G. H. Bryan, K. Ikeda, S. A. Tessendorf, and G. Thompson. 2015. Parameterization of cloud microphysics based on the prediction of bulk ice particle properties. Part II: Case study comparisons with observations and other schemes. *Journal of Atmospheric Sciences* 72, 1 (2015), 312–339.
- A. Nemes and W. J. Rawls. 2004. Soil texture and particle-size distribution as input to estimate soil hydraulic properties. *Developments in soil science* 30 (2004), 47–70.
- F. Neyret. 1997. Qualitative Simulation of Convective Cloud Formation and Evolution. In *Computer Animation and Simulation '97*, D. Thalmann and M. van de Panne (Eds.). Springer Vienna, Vienna, 113–124.
- D. Overby, Z. Melek, and J. Keyser. 2002. Interactive physically-based cloud simulation. In *10th Pacific Conference on Computer Graphics and Applications, 2002. Proceedings*. 469–470.
- M. Padilla, A. Chern, F. Knöppel, U. Pinkall, and P. Schröder. 2019. On Bubble Rings and Ink Chandeliers. *ACM Trans. Graph.* 38, 4, Article 129 (July 2019), 14 pages.
- K. Perlin. 1985. An image synthesizer. *ACM Siggraph Computer Graphics* 19, 3 (1985), 287–296.
- M. Pharr, W. Jakob, and G. Humphreys. 2016. *Physically based rendering: From theory to implementation*. Morgan Kaufmann.
- S. Pirk, T. Jarzabek, M. Hädrich, D. L. Michels, and W. Palubicki. 2017. Interactive Wood Combustion for Botanical Tree Models. *ACM Trans. Graph.* 36, 6, Article 197 (Nov. 2017), 12 pages.
- S. Pirk, T. Niese, T. Hädrich, B. Benes, and O. Deussen. 2014. Windy Trees: Computing Stress Response for Developmental Tree Models. *ACM Trans. Graph.* 33, 6, Article 204 (Nov. 2014), 11 pages.
- F. Pithan, B. Medeiros, and T. Mauritsen. 2014. Mixed-phase clouds cause climate model biases in Arctic wintertime temperature inversions. *Climate dynamics* 43, 1-2 (2014), 289–303.
- H. R. Pruppacher and J. D. Klett. 2012. *Microphysics of Clouds and Precipitation: Reprinted 1980*. Springer Science & Business Media.
- R. M. Rasmussen and A. J. Heymsfield. 1987. Melting and shedding of graupel and hail. Part I: Model physics. *Journal of Atmospheric Sciences* 44, 19 (1987), 2754–2763.
- S. Ravichandran, E. Meiburg, and R. Govindarajan. 2020. Mammatus cloud formation by settling and evaporation. *Journal of Fluid Mechanics* 899 (2020), A27.
- T. Reed and B. Wyvill. 1994. Visual Simulation of Lightning. In *Proceedings of the 21st Annual Conference on Computer Graphics and Interactive Techniques (SIGGRAPH '94)*. Association for Computing Machinery, New York, NY, USA, 359–364.
- B. Ren, J. Huang, M. C. Lin, and S.-M. Hu. 2018. Controllable dendritic crystal simulation using orientation field. In *Computer Graphics Forum*, Vol. 37. Wiley Online Library, 485–495.
- H. Richner and P. Hächler. 2013. Understanding and forecasting Alpine foehn. In *Mountain Weather Research and Forecasting*. Springer, 219–260.
- P. J. Ross and J.-Y. Parlange. 1994. Comparing exact and numerical solutions of Richard's equation for one-dimensional infiltration and drainage. *Soil science* 157, 6 (1994), 341–344.
- L. D. Rotstain. 1997. A physically based scheme for the treatment of stratiform clouds and precipitation in large-scale models. I: Description and evaluation of the microphysical processes. *Quarterly Journal of the Royal Meteorological Society* 123, 541 (1997), 1227–1282.
- L. D. Rotstain, B. F. Ryan, and J. J. Katzfey. 2000. A scheme for calculation of the liquid fraction in mixed-phase stratiform clouds in large-scale models. *Monthly weather review* 128, 4 (2000), 1070–1088.
- S. A. Rutledge and P. Hobbs. 1983. The mesoscale and microscale structure and organization of clouds and precipitation in midlatitude cyclones. VIII: A model for the “seeder-feeder” process in warm-frontal rainbands. *Journal of Atmospheric Sciences* 40, 5 (1983), 1185–1206.
- S. A. Rutledge and P. V. Hobbs. 1984. The mesoscale and microscale structure and organization of clouds and precipitation in midlatitude cyclones. XII: A diagnostic modeling study of precipitation development in narrow cold-frontal rainbands. *Journal of Atmospheric Sciences* 41, 20 (1984), 2949–2972.
- J. Schalkwijk, H. J. J. Jonker, A. P. Siebesma, and E. Van Meijgaard. 2015. Weather forecasting using GPU-based large-eddy simulations. *Bulletin of the American Meteorological Society* 96, 5 (2015), 715–723.
- P. Schultz. 1995. An explicit cloud physics parameterization for operational numerical weather prediction. *Monthly weather review* 123, 11 (1995), 3331–3343.
- M. A. Shirazi, L. Boersma, and J. W. Hart. 1988. A unifying quantitative analysis of soil texture: improvement of precision and extension of scale. *Soil Science Society of America Journal* 52, 1 (1988), 181–190.
- H.-J. Song and B.-J. Sohn. 2018. An evaluation of WRF microphysics schemes for simulating the warm-type heavy rain over the Korean peninsula. *Asia-Pacific Journal of Atmospheric Sciences* 54, 2 (2018), 225–236.
- R. C. Srivastava. 1967. A study of the effect of precipitation on cumulus dynamics. *Journal of Atmospheric Sciences* 24, 1 (1967), 36–45.
- R. C. Srivastava. 1971. Size distribution of raindrops generated by their breakup and coalescence. *Journal of Atmospheric Sciences* 28, 3 (1971), 410–415.
- J. Stam. 1999. Stable Fluids. *Proc. of ACM SIGGRAPH* (1999), 121–128.
- J. Steinhoff and D. Underhill. 1994. Modification of the Euler equations for “vorticity confinement”: Application to the computation of interacting vortex rings. *Physics of Fluids* 6, 8 (1994), 2738–2744.
- T. Stocker. 2011. *Introduction to Climate Modeling*. Springer-Verlag Berlin Heidelberg.

- A. Stomakhin, C. Schroeder, C. Jiang, L. Chai, J. Teran, and A. Selle. 2014. Augmented MPM for phase-change and varied materials. *ACM Transactions on Graphics (TOG)* 33, 4 (2014), 1–11.
- J. M. Straka. 2009. *Cloud and precipitation microphysics: principles and parameterizations*. Cambridge University Press.
- S. Trömel, A. V. Ryzhkov, M. Diederich, K. Mühlbauer, S. Kneifel, J. Snyder, and C. Simmer. 2017. Multisensor characterization of mammatus. *Monthly Weather Review* 145, 1 (2017), 235–251.
- K. Um, X. Hu, and N. Thürey. 2018. Liquid Splash Modeling with Neural Networks. *CGF* 37, 8 (2018), 171–182.
- B. Ummenhofer, L. Prantl, N. Thürey, and V. Koltun. 2020. Lagrangian Fluid Simulation with Continuous Convolutions. In *ICLR*.
- U. Vimont, J. Gain, M. Lastic, G. Cordonnier, B. Abiodun, and M.-C. Cani. 2020. Interactive Meso-scale Simulation of Skyscapes. *Eurographics* (2020).
- E. M. Volodin, N. A. Dianskii, and A. V. Gusev. 2010. Simulating present-day climate with the INMCM4. 0 coupled model of the atmospheric and oceanic general circulations. *Izvestiya, Atmospheric and Oceanic Physics* 46, 4 (2010), 414–431.
- A. Webanck, Y. Cortial, E. Guérin, and E. Galin. 2018. Procedural cloudscape. In *Computer Graphics Forum*, Vol. 37. Wiley Online Library, 431–442.
- T. Wu, R. Yu, F. Zhang, Z. Wang, M. Dong, L. Wang, X. Jin, D. Chen, and L. Li. 2010. The Beijing Climate Center atmospheric general circulation model: description and its performance for the present-day climate. *Climate dynamics* 34, 1 (2010), 123.
- Y. Xie, E. Franz, M. Chu, and N. Thürey. 2018. TempoGAN: A Temporally Coherent, Volumetric GAN for Super-Resolution Fluid Flow. *ACM Trans. Graph.* 37, 4, Article 95 (2018), 15 pages.
- T. Xue, H. Su, C. Han, C. Jiang, and M. Aanjaneya. 2020. A novel discretization and numerical solver for non-fourier diffusion. *ACM Transactions on Graphics (TOG)* 39, 6 (2020), 1–14.
- M. K. Yau and R. R. Rogers. 1996. *A short course in cloud physics*. Elsevier.
- L. Yu. 2007. Global variations in oceanic evaporation (1958–2005): The role of the changing wind speed. *Journal of climate* 20, 21 (2007), 5376–5390.

## A LIST OF SYMBOLS

$A_C$	Autoconversion of cold cloud into snow.
$A_W$	Autoconversion of warm cloud into rain water.
$B_W$	Conversion of warm cloud into cold cloud via the WBF process.
$C_W$	Condensation of vapor into warm cloud.
$D_C$	Deposition of vapor into cold cloud.
$E_G$	Evaporation from the ground.
$E_I$	Evaporation of precipitated ice.
$E_R$	Evaporation of rain water.
$E_S$	Evaporation of snow.
$E_W$	Evaporation of warm cloud.
$F_R$	Freezing of rain water into precipitated ice.
$F_W$	Freezing of warm cloud into cold cloud.
$G_I$	Precipitated ice that has reached the ground.
$G_R$	Rain that has reached the ground.
$G_S$	Snow that has reached the ground.
$I_R$	Infiltration of rain into the ground.
$K_C$	Accretion of cold cloud by snow.
$K_W$	Accretion of warm cloud by rain water.
$M_C$	Melting of cold cloud into warm cloud.
$M_I$	Melting of precipitated ice into rain water.
$M_S$	Melting of cold cloud into warm cloud.
$R_S$	Rimming of snow into precipitated ice.
$R_W$	Rimming of warm cloud into precipitated ice.
$S_C$	Sublimation of cold cloud.

## B DERIVATION OF TERMINAL SPEEDS

The diameter of precipitation particles is assumed to follow an exponential distribution

$$\begin{aligned} n_R(D) &= n_{0R} \exp[-\lambda_R D_R], \\ n_S(D) &= n_{0S} \exp[-\lambda_S D_S], \\ n_I(D) &= n_{0I} \exp[-\lambda_I D_I], \end{aligned}$$

where  $n_{0R}$ ,  $n_{0S}$  and  $n_{0I}$  are the intercept parameters of the rain, snow and precipitated ice diameter distributions, respectively. According to measurements made by Srivastava [1971], Gunn and Marshall [1958], and Auer [1972], we set  $n_{0R} = 8 \cdot 10^{-2} \text{ cm}^{-4}$ ,  $n_{0S} = 3 \cdot 10^{-2} \text{ cm}^{-4}$ , and  $n_{0I} = 4 \cdot 10^{-4} \text{ cm}^{-4}$ . The slope parameters  $\lambda_{R,S,I}$  are determined by multiplying the corresponding distribution with the particle mass, integrating over all diameters, and equating the resulting quantity to water/ice content. We obtain

$$\begin{aligned} \lambda_R &= \left( \frac{\pi \rho_{\text{water}} n_{0R}}{\rho_{\text{air}} q_r} \right)^e, & \lambda_S &= \left( \frac{\pi \rho_{\text{snow}} n_{0S}}{\rho_{\text{air}} q_s} \right)^e, \\ \lambda_I &= \left( \frac{\pi \rho_{\text{ice}} n_{0I}}{\rho_{\text{air}} q_i} \right)^e \end{aligned}$$

with  $e = 0.25$  and densities  $\rho_{\text{water}} = 0.99 \text{ g cm}^{-3}$ ,  $\rho_{\text{snow}} = 0.11 \text{ g cm}^{-3}$ , and  $\rho_{\text{ice}} = 0.91 \text{ g cm}^{-3}$ . Based on the measurements of Locatelli and Hobbs [1974], the terminal velocities for precipitation particles of a given diameter are

$$\begin{aligned} U_{DR} &= a D_R^b \sqrt{\frac{\rho_{\text{water}}}{\rho_{\text{air}}}}, & U_{DS} &= c D_S^d \sqrt{\frac{\rho_{\text{snow}}}{\rho_{\text{air}}}}, \\ U_{DI} &= \sqrt{\frac{4}{3 C_D}} D_G^{1/2} \sqrt{\frac{g \rho_{\text{ice}}}{\rho_{\text{air}}}} \end{aligned}$$

with constants  $a = 2115 \text{ cm}^{1-b} \text{ s}^{-1}$ ,  $b = 0.8$  [et al. 1997],  $c = 152.93 \text{ cm}^{1-d} \text{ s}^{-1}$ ,  $d = 0.25$  [Locatelli and Hobbs 1974], and drag coefficient  $C_D = 0.6$  [Rasmussen and Heymsfield 1987]. Following Srivastava [1967] we define the mass-weighted mean terminal velocity as

$$U_j = \int U_{Dj} q_j(D) dD / q_j$$

with the terminal velocity  $U_{Dj}$  of precipitation types  $j$  and mixing ratio  $q_j(D)$  of a particle of diameter  $D$ . By integrating this functions we obtain the mass-weighted mean terminal velocities.

## C PARAMETER SPACE EXPLORATION

We present a parameter space exploration in Figure 19 systematically varying the average solar irradiance  $\bar{P}$  and the water content  $\bar{q}_{sr}$ .

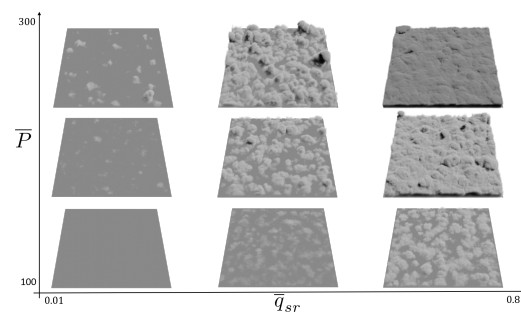


Fig. 19. Parameter space exploration varying average solar irradiance  $\bar{P}$  and water content  $\bar{q}_{sr}$ . The initial ground temperature is set to  $T_G = 21^\circ \text{C}$ , the elapsed time is  $t = 6 \text{ h}$ , and the ground type is set to loam:  $\gamma_1 = 0.4$ ,  $\gamma_2 = 0.4$ ,  $\gamma_3 = 0.2$ , and  $\gamma_{\text{perlin}} = 0.05$ .